

FINAL REPORT

Project: H44-T117-2004

**Modeling Activities at UAH in Support of TexAQSI
TASKS 1, 2 & 3**

**Covering the Period of
October 2004 to August 2005**

**Submitted to the
Houston Advanced Research Center (HARC)**

Investigators:

**Arastoo Pour Biazar,
Richard T. McNider,
Kevin Doty,
William B. Norris,
Don Moss**

**Earth System Science Center
University of Alabama in Huntsville**

August 2005

Table of Contents

1. INTRODUCTION	1
2. GOES Data Assimilation in Support of TexAQSII	1
2.1. GOES Data Assimilation in MM5.....	1
2.2. GOES Data Assimilation in CMAQ.....	3
2.2.1. Results.....	5
3. Web-Based Lagrangian Particle Model.....	9
3.1. Technical Details & Model Physics	9
3.1.1. Background of Theoretical Formulation.....	9
3.1.2. Formulation of Turbulent Wind Deviations and Lagrangian Time Scales With Monin-Obukhov Similarity Theory.....	10
3.1.3. Formulations for the Stable Case.....	11
3.1.4. Formulations for the Neutral Case.....	11
3.1.5. Formulations for the Unstable Case.....	11
3.1.6. Formulations for the Lagrangian Autocorrelation Functions	12
3.1.7. Formulations for the Parameterized Turbulent Velocity Components.....	13
3.1.8. Approach Used Above the PBL.....	13
3.1.9. Trajectory Calculation Procedures.....	14
3.1.10. Plume Rise Calculation Procedures.....	15
3.2. Data Transfer Issues	17
3.3. Model Benefits for Field Study	20
3.4. Features of the Web-Based Version	21
3.4.1. Current Features.....	21
3.4.2. Features Planned for the Upgraded Version.....	21
4. Field Program Planning	22
4.1. Lagrangian Multi-particle Simulation for interpretation of Tetroon Releases	22
4.2. Interpretation of Role of Inhomogeneous Wind Fields.....	24
5. REFERENCES	32
6. Figures.....	33

1. INTRODUCTION

The following is the final report for tasks 1, 2 and 3 of project *H44.T117.2004*, “Modeling Activities at UAH in Support of TexAQSII,” summarizing the activities for the period of October 2004 to August 2005. This report summarizes the new activities as well as recounting the activities summarized in the interim reports submitted for the above tasks.

Overall while we encountered many difficulties in several areas, we have been able to meet the deadlines set for the 2005 field campaign. In the following we summarize our activities under each task and provide some of the technical details where it is necessary.

2. TASK 1: GOES Data Assimilation in Support of TexAQS II

The objective of this task is the use of GOES data assimilation to improve the prediction of boundary layer characteristics and air quality simulations. Two main components of this task are the continuation of our work with respect to the assimilation of GOES observed cloud information in CMAQ and the assimilation of GOES retrievals in MM5.

2.1 GOES data assimilation in MM5:

Our GOES data assimilation effort is the continuation of our earlier attempts in utilizing GOES skin temperature retrievals, together with the retrievals of surface insolation and albedo to correct model physical parameters in order to improve model predictions of the boundary layer characteristics.

Our previous work had indicated that using satellite assimilation made an overall improvement in the performance of MM5 with respect to the predictions of critical boundary layer variables. With the use of this technique, model-predicted skin temperatures exhibited a better agreement with the satellite retrieved skin temperatures. The comparison of the model-predicted surface layer temperatures to National Weather Service (NWS) 2-m observations also indicated considerable improvements. The use of satellite assimilation also improved the prediction of boundary layer heights as evident from comparisons made to the limited observations during TexAQS2000 study. Despite these improvements, a more detailed evaluation of the model results indicated that there could be problems with the flux terms in the surface energy budget.

The other shortcoming of the model was that (due to our modifications/additions to MM5) the modified code could not take advantage of multiple processors on a distributed memory platform and had to be run on a single processor. This was due to the fact that the MPP option of MM5 reorganizes and rewrites the source code before compile step. This requires that any addition/modification to the code be known to the preprocessors and be consistent with their requirements. Being limited to using only one processor was limiting the use of the modified code. For example we were not able to use the modified code for real-time forecasting if needed during 2005 and 2006 Texas campaigns. We were also limited in the number of sensitivity runs we could make for large high-resolution domains. Therefore a major task under this project was to modify the satellite

assimilation code (hereafter referred to as MM5/GOES) for parallel processing while continuing the evaluation of the satellite assimilation technique to address the issue of warm/dry bias of the technique.

The MM5/GOES code used at the start of this task was based on MM5/version 3.4. In the preparation of the code for parallel processing we encountered many unforeseen problems. Many of the new modifications we made to the model required changes in the other parts of the modeling system. This was due to the additions we have made to the code to correct heat capacity (utilizing evening retrieved tendencies), the addition of a new soil option, the introduction of a new diffusion solver in slab, and addition of new options in the deck-file. Many of these changes were not documented and therefore the task of finding the possible conflicts with the MPP option proved to be a challenging task. After our initial attempts failed at producing a desirable result, we finally concluded that it was better to start from a clean version of standard MM5 release and add the necessary changes for satellite assimilation to the code. This way, we could make sure that we avoid any conflict with the standard structure of the model. Since this required redoing many code changes that we had made in the past several years, we also decided to implement the changes to the latest release of MM5 so that we will have the most up-to-date version of the model.

Therefore, we started our second attempt at parallelization by acquiring version 3.7.2 of MM5 and implementing the satellite assimilation changes accordingly. In doing so we revisited all the changes and inserted additional comments in the code to reflect the purpose of each change and make the detection of our modifications easier. We also found few instances of inconsistency in memory allocation that we corrected.

Having made these changes, the next step was to make corresponding modifications to the MPP code. After performing the appropriate changes we still had problem with the loop indices. The Fortran loop and index converter (FLIC) completely changes the computational grid and as a result the memory allocation in routines are altered. This was causing problems for us as far as initialization and IO was concerned. We finally were able to get the modified code to compile and run on parallel processors.

Our approach for testing the performance of the parallel code was to compare the results to the single processor run in each case. We started with a simulation without activating assimilation options using the modified code. Then we continued by several runs using different combinations for assimilation (i.e., only moisture availability adjustment, only heat capacity adjustment, and both). The purpose of this practice was not to use the results for any analysis, but to make sure that the parallel version will produce the same results and that there are not problems in memory allocation and the flow of the information within the model.

Analyzing the results we noticed large differences between the single processor run and the parallel version. We investigated the cause of the discrepancy by looking for problems in our modifications to the code. This was based on the assumption that for the standard version of MM5 (version 3.72) a parallel simulation would produce similar

results as a single processor simulation (within a reasonable margin of error). We later decided to test this assumption.

Unfortunately, we realized that the above assumption was not correct. Figure 9 exhibits the difference between a run done on a single processor and one using the MPP option and using 4 processors. As evident in the figure the maximum absolute errors for u-component of horizontal wind show an increasing trend with a maximum of 5 m/s. The maximum for relative error initially was substantially higher than what is shown in the figure. This was due to large relative errors for relatively calm situation. Since high relative errors due to near-zero wind speeds are not as important in the simulation, we decided to filter the relative errors for low wind speeds. Exhibited in figure 9 are the maximum absolute relative errors for wind speeds greater than 1 cm/s. Even with filtering out errors for low wind speeds, the relative errors can reach a value of 70%. The lower two panels in Figure 9 show the propagation of errors in space and time. The plots show the fraction of the grid points in the domain that experience relative errors of 5% (and 10%) and greater. As evident from the plots, the number of grids experiencing significant error increases as the simulation proceeds. The plots also indicate that while the grid points experiencing very large errors are limited in number, a substantial number of grids experience errors on the order of 5 to 10% which is significant. We are in the process of investigating the cause of such a large difference.

Similar pattern in errors can be seen when examining other variables. Figures 10 and 11 show the errors in u-component for a similar comparison as in the standard MM5 but for the modified code. Figure 10 presents the errors from a run in which satellite assimilation options were not activated and Figure 11 is from a run in which moisture availability was adjusted based on satellite retrieved skin temperature tendencies. The errors are comparable to the standard run and at this point we think that the modifications are not introducing any new error in the model. Our task now is to find out why there are such errors in the standard MM5. We have communicated these results to MM5 users' community and to the MM5 help desk. We have not received any helpful feed back yet. We are in the process of taking a methodical approach in resolving this problem. Starting from the single processor run we will be adding additional processors gradually and will be examining the compiler switches.

2.2 GOES data assimilation in CMAQ:

Photolysis rates depend on the amount of solar radiation reaching a given point in the atmosphere and the molecular properties of the molecule undergoing photodissociation. Therefore, attenuation or enhancement of radiant energy due to atmospheric absorption and scattering is an important factor in determining the photolysis rates. Since clouds can significantly alter the solar radiation in the wavelengths affecting the photolysis rates, they can have considerable impact on the photochemistry. Unfortunately, in current modeling systems, there are major problems with estimating cloud corrections to photolysis fields. Use of observed cloud information impacts any area where there is a discrepancy between MM5-predicted and observed cloud fields and would be able to correct both over- and under-predictions that result from cloud correction in CMAQ.

We utilize GOES observed cloud information in the Community Multiscale Air Quality modeling system [CMAQ, EPA, 1999] to correct photolysis rates for observed clouds. CMAQ uses a two-step approach for calculating the photolysis rates. This approach is similar to that of Regional Acid Deposition Model [RADM, Chang et al., 1987] and is a typical method used in most off-line air quality models. First, in a preprocessor, a radiative transfer module [based on Madronich, 1987] is used to compute clear sky photolysis rates for a range of latitudes, altitudes, and zenith angles. Then, within the chemical transport model, the tabular photolysis rates are interpolated for each location and corrected for cloud cover. There are two major concerns with this approach as far as cloud correction is concerned. First, estimation of cloud transmissivity in models is highly parameterized and therefore introduces a large uncertainty. Second and most importantly, the cloud information is provided by a mesoscale model, which has difficulty with the spatial and temporal placement of clouds and their vertical extent. The mesoscale model used in CMAQ modeling system is the Fifth-Generation Penn State/NCAR Mesoscale Model (MM5) [Grell et al., 1994; NCAR, 2003].

Photolysis rate (s^{-1}) is represented by:

$$J = \int_{\lambda_1}^{\lambda_2} \sigma(\lambda) \phi(\lambda) F(\lambda) d\lambda \quad (1)$$

Where $\sigma(\lambda)$ ($m^2/molecule$) is the absorption cross-section for the molecule undergoing photodissociation as a function of wavelength λ (μm); $\phi(\lambda)$, quantum yield ($molecules/photon$), is the probability that the molecule photodissociates in the direction of the pertinent reaction upon absorbing the radiation of wavelength λ ; and $F(\lambda)$ is the actinic flux ($photons/m^2/s/\mu m$).

By providing the actinic flux for clear sky, photolysis rates (J_{clear}) can be calculated by equation (1). In CMAQ, following Chang et al. (1987) and Madronich (1987), these rates are corrected for cloud cover. Below the cloud, the rate is corrected by:

$$J_{below} = J_{clear} [I + f_c (1.6 tr_c \cos(\theta) - I)] \quad (2)$$

Where f_c is the cloud fraction for a grid cell, tr_c is cloud transmissivity, and θ is the zenith angle. The above formulation leads to a lower value for the photolysis rates below the cloud, where the cloud transmissivity is reduced. Above the cloud, photolysis rate is modified as:

$$J_{above} = J_{clear} [I + f_c \alpha \cos(\theta) (I - tr_c)] \quad (3)$$

Here α is a reaction dependent coefficient that further modifies above the cloud enhancement (Chang et al., 1987). This is to allow for the photolysis rate enhancement that is resulting from the reflected radiation from the cloud top. Within the cloud, the photolysis rates are obtained by interpolating between cloud base and cloud top values. Therefore, based on the formulation above, the cloud transmittance and cloud fraction are required for calculating cloud correction for photolysis rates. Also, since in-cloud photolysis rates are interpolated, cloud base and top heights must also be known.

In CMAQ, the calculation of cloud transmissivity is highly parameterized. The formulation is based on the parameterization suggested by Stephens (1978). By

obtaining cloud thickness (H_c) and liquid water content (w) from MM5, liquid water path (g/m^2) is calculated by:

$$LWP = wH_c \quad (4)$$

Then the broadband cloud optical depth (τ_c) as a function of liquid water path is calculated as:

$$\tau_c = 10^{2.633+1.7095 \ln[\log_{10}(LWP)]} \quad (5)$$

Finally, assuming a scattering phase-function asymmetry factor of .86, cloud transmissivity is calculated by:

$$tr_c = \frac{5 - e^{-\tau_c}}{4 + 3\tau_c(1 - \beta)} \quad (6)$$

Where β is the scattering phase-function asymmetry factor. As evident from the above formulation, even if the MM5 cloud prediction was correct, there is a large uncertainty in the above calculation of cloud transmittance due to the assumptions used in the parameterization.

From GOES satellite observations, we are able to recover broadband cloud transmissivity and the cloud top height. Also, since GOES cloud mask algorithm can detect clouds at 4-km resolution, an observed cloud fraction can be calculated for coarser grid cells as the fraction of cloudy pixels within a grid cell. Cloud base height is estimated as the local condensation level (LCL) from the information (temperature and mixing ratio fields) provided by the mesoscale model. In this study we replaced tr_c and f_c in equations (2) and (3) with the satellite inferred quantities to perform the cloud correction.

We added another component to Meteorology-Chemistry Interface Processor (MCIP) for calculation of cloud base height from MM5 moisture and temperature information. Previously the cloud base height was set to a constant value regardless of the atmospheric conditions. We compute lifting condensation level by iteration using a variation of Poisson's equation:

$$T_c = B / \ln \left[\frac{A \varepsilon \left(\frac{T_0}{T_c} \right)^{1/k}}{w p_0 \left(\frac{T_c}{T_0} \right)} \right]$$

Where $B=5.42 \times 10^3$ K, and $A=2.53 \times 10^8$ kPa are the empirical constants and $\varepsilon = R'/R_v = 0.622$, where R' is the gas constant for dry air ($287 \text{ J kg}^{-1} \text{ K}^{-1}$) and R_v is the gas constant for water vapor ($461.5 \text{ J kg}^{-1} \text{ K}^{-1}$). w , p_0 , and T_0 are near surface mixing ratio, pressure, and temperature respectively.

2.2.2 Results

GOES data assimilation in CMAQ, partly supported under the current HARC funding, started under an earlier funding through Lamar University. The results presented here therefore complement the earlier reports submitted to the State of Texas through Lamar University.

The technique described above was implemented in the CMAQ modeling system to perform a set of simulations for 12- and 4-km resolution domains over Texas for the period of August 24 to August 31, 2000. The 12-km domain covers the eastern half of Texas, Louisiana, Mississippi, southern part of Oklahoma and Arkansas, and the southwestern corner of Tennessee. The first set of simulations utilized CMAQ in its standard configuration, and is used as the control case (hereafter referred to as CMAQ_base) for comparison. The second set of simulations (hereafter referred to as CMAQ_sat) used the satellite observed cloud information. Both sets of simulations use the same meteorological information from a single MM5 run.

The control MM5 simulation was configured to use FDDA gridded nudging, Dudhia moisture scheme, Grell convective parameterization, Medium Range Forecast (MRF) PBL scheme, RRTM radiation scheme, shallow convection scheme, and 5-layer soil model. Grell cumulus parameterization has proven to be useful for smaller grid sizes (10-30 km). It tends to allow a balance between resolved scale rainfall and convective rainfall.

CMAQ (version 4.3) was configured to use piecewise parabolic method for advection, multiscale horizontal diffusion and eddy vertical diffusion, SMVGEAR chemical solver, 3rd generation aerosol model and 2nd generation aerosol deposition model, RADM cloud model, and SMVGEAR chemical solver. Carbon bond IV (CB4) chemical mechanism (Gery et al., 1989), including aerosol and aqueous chemistry was utilized to describe atmospheric reactions. The model uses 21 layers, with about 10 layers within the daytime boundary layer. The emissions for this study are based on EPA's 1999 National Emissions Inventory (NEI99, version 2).

Since the meteorological information was obtained from a single MM5 simulation, there is no change in the dynamic fields for the CMAQ simulations and the differences between CMAQ_base and CMAQ_sat simulations are only due to the impact of observed clouds on the photochemistry. It should be noted, however, that the uncertainty in the standard modeling results could be even greater due to the impact of cloud dynamics on the vertical transport of the pollutants.

For example, on the afternoon of August 24, convective clouds developed over the Galveston Bay and expanded toward north/northwest. This is absent in the MM5 simulation, meaning that the vertical transport of pollutants over the Bay area into these convective cells is missing in our simulations. While our method corrects for the impact of the observed convective clouds on the photochemistry, there are still errors arising from the lack of accurate distribution of pollutants due to errors in the dynamics. Therefore, a model-to-model comparison would be able to illustrate the first-order photochemical impact of including the observed clouds.

Moreover, during the period of our study, Texas and surrounding areas were extremely dry and perhaps not the best case to show the benefits of utilizing GOES information. Nevertheless, there was enough cloudiness to show the impact of observed clouds on the photochemical model predictions.

The overall spatial distribution (on a large scale) of the predicted ozone for both the control and satellite assimilation simulations generally agree with observations. Figures 13 and 14 depict snapshots of the CMAQ predictions at 21:00 and 22:00 GMT on August 24, 2000. The model is able to predict the low ozone concentrations next to the Houston-Galveston Bay as well as the high ozone concentrations in the Dallas area. However, model predictions of high ozone concentrations in many rural areas cannot be substantiated due to the large gaps in the observational network.

Figure 12 exhibits the largest differences (in absolute value) in ozone, and NO_x between the two simulations for the 12-km domain. The figure represents the extreme cases of discrepancy between control and assimilation simulations, and these extremes may not occur at the same time. However, the larger values probably represent the same time period, as the negative/positive values for NO are co-located with the positive/negative values of NO₂. The areas marked with a large negative NO difference between the assimilation and control correspond to the situation where MM5 predicts cloud, where in fact there is no cloud in the observation and therefore most of NO is converted to NO₂ (and vice versa). These areas are confined to the large source regions as evident for example over the Houston-Galveston Bay area indicating a much faster photochemical activity and rapid ozone formation.

For the NO₂ case there are broader areas of large discrepancy. Over the Texas region, this indicates the transport of NO_x outside the source region where the lifetime of NO₂ is increased. This is perhaps due to the transport and dilution of the air mass outside the source region and mixing with an air mass of lower VOC where the rapid ozone formation is inhibited. The evidence for this statement can be seen in Figure 12a where the extreme ozone differences are depicted.

This figure also indicates that there are times that the impact of our method on ozone concentration can be quite high (as much as 60 ppb). While these extreme cases are mostly localized in space and time, sustained differences of several ppb over broader areas are more common. Comparing the extreme values of NO_x and ozone, there is a good correlation between higher ozone concentrations in the assimilation run and lower NO_x concentrations (and lower NO₂ concentrations). This indicates the presence of observed clear sky in contrast to MM5 over-predictions of clouds. Therefore the assimilation run produces more ozone and nitrates at the expense of NO_x. On the other hand, under-predictions of clouds in MM5 resulted in higher ozone values in the control run for the east/southeast and northern part of Louisiana and a large part of central Texas.

As indicated in Figure 12, the impact of alterations in the photolysis rates on the local atmospheric chemical composition can be substantial, especially on the chemical species with the shorter photochemical lifetime. It should be noted, however, that the domain averaged differences only show a maximum of 2 ppb for August 26 and are mostly between +/- 1 ppb for other days. They also exhibit a diurnal variation with higher predicted ozone for the assimilation run.

On August 24, 2000, MM5 predicts clouds to the south/southeast of the domain with most of it being subgrid scale. Only few small areas of grid scale clouds over land are predicted. In contrast, satellite observations indicated large area of cloudiness extending from south/southeast to the northwest part of the domain. Satellite observation also indicated clouds in the northeast and northern parts of the domain that are absent in the MM5 predictions. However, the broadband transmissivity for most of the observed clouds for this day is high, meaning that most of the clouds are not thick and will not affect the photolysis rates significantly. But the area around Galveston Bay, including Houston, was covered with thick clouds and was missing in the MM5 predictions. This is significant, as this area is the major source of emissions for ozone precursors.

An error in the prediction of thick clouds over the emissions sources has major consequences. Thick clouds can significantly alter the cloud transmissivity and thus the photolysis rates. Over the source regions, an alteration (reduction in this case) in the photolysis rate has both a direct and an indirect impact on ozone chemistry. First, by slowing down the photochemistry, lower photolysis rates inhibit ozone production in the immediate vicinity of emissions sources (direct impact). Second, due to the suppression of photochemistry, lifetime of ozone precursors is increased and the precursors can be transported to the regions where the air mass has a different chemical composition (indirect impact). In the case of Galveston Bay region, since NO_x and VOCs are co-emitted, the inhibition of the photochemistry directly impacts the rapid formation of ozone in this area. By doing so, both NO_x and VOC remain active for a longer period of time and are transported out of the area. In short, such an event alters the chemical aging of the air mass, and the air mass continues to have the potential of producing ozone for a longer period of time during transport.

Another indirect impact of this scenario is the alteration in partitioning of nitrogen oxides and the impact on nitrate budget due to surface deposition losses. In the presence of thick clouds over the emissions sources of NO_x, nitrogen monoxide rapidly consumes ozone and produces nitrogen dioxide. Therefore, while the partitioning of NO_x between NO and NO₂ has been altered, there is a net increase in NO_x. Due to the slow down in the photochemistry, most of the NO_x will remain intact and will not be lost in the ozone production to produce nitrates. The major loss for NO_x in this situation is the surface removal, and the rate of surface removal for NO_x is an order of magnitude less than that of nitric acid (HNO₃) [Biazar, 1995]. Therefore, in the absence of clouds over the Galveston Bay area in the control case, there is a much larger loss of total nitrogen oxides (NO_y) due to surface removal. Examining a grid point close to the bay (southeast of Houston at 29.7N, 95.3W) reveals that the absence of clouds increased the surface removal of HNO₃ for several hours for up to 9 ppb. The loss positively correlates with the increased ozone production and is the result of increased HNO₃ production due to active photochemistry. The inclusion of clouds resulted in less than 1 ppb loss of NO_x in this case.

In contrast to the August 24 case, on August 28, MM5 predicts a large area of cloudiness over western Mississippi, southern Arkansas, and Louisiana extending to the south Texas. This is absent in the GOES observation. GOES observations indicate subgrid cloudiness

to the western part of Texas. Transmissivity retrievals, however, indicate that these clouds are highly transparent and do not alter the photolysis rates significantly. Therefore in this case we have a significant ozone formation in the vicinity of the emission sources that would be absent in the control simulation.

3. TASK 2: WEB-BASED LAGRANGIAN PARTICLE MODEL

Under task 2 of this project UAH was responsible for the creation of a Web-based operational Lagrangian particle model to be available for TexAQSI II planning briefings and also for use by the scientists during the study period.

This task has been accomplished and the web site can be accessed at <http://TexAQSI2.nsstc.uah.edu>. The site is operational and is currently being used by scientists during the 2005 field study. In the following we first summarize the underlying physics of the model and its benefits as an air-quality field study tool. Then we discuss its current and future features.

3.1. Technical Details & Model Physics

Based on conditioned particle concepts (Smith, 1968) in which the Lagrangian turbulent velocity fluctuation of a non-buoyant tracer particle is linearly related to the turbulent fluctuation of the previous time step, the model deduces subgrid-scale velocities (turbulence) from the mean flow parametrically. Unlike simpler models, which use only mean flow to compute a single trajectory, the LPM simultaneously computes the trajectories of many particles. By accounting for the effects of both the mean flow and turbulence on each particle, the model is able to depict both transport and dispersion of plumes.

The following discussion gives a survey of the theory and practical issues surrounding the transfer of MM5 data from Texas A&M University (TAMU) to the University of Alabama at Huntsville (UAH) that supplies the input data for a Lagrangian Particle Model (LPM) which has an interactive web page. Section 3.1.1 gives the background on the theory the LPM utilizes. Section 3.1.2 provides the equations used for the Lagrangian time scales and the standard deviation of the respective wind components for regions within the planetary boundary layer (PBL) and then above it. The subsequent sections give some details on the actual trajectory calculation procedures, and section 3.1.10 discusses the plume rise equations used for a “hot” source. Finally, section 3.2 gives some details of the data flow between (TAMU) and (UAH).

3.1.1. Background of theoretical formulation

Smith (1968) introduced the idea of parameterizing turbulent components with a linear Markov model, which as an example for the u component direction would be like (1), which makes the current turbulent component at time “t” a function of an earlier turbulent component in a Lagrangian sense times an Lagrangian autocorrelation function plus a random component u’.

$$u'(t) = u'(t - \Delta t_s) R_u + u'' \quad (1)$$

Hanna (1979) utilized Lagrangian and Eulerian wind data (including tetron flights) to show that (1) was a legitimate model. Pielke et al. (1983) utilized (1) in the context of a Lagrangian particle model (LPM) utilizing the output of a mesoscale model. The LPM used in this study is based on the same approach. A summary of all symbols used in the following discussion is provided in Table 1.

3.1.2 Formulation of turbulent wind deviations and Lagrangian time scales with Monin-Obukhov similarity theory

Equations (2)-(4) give the standard formulation of the Monin-Obukhov similarity (MOS) characteristic scales of momentum, heat, and water vapor, respectively. The formulation of the moisture scale Q^* can be significantly different from (4) depending on the degree of complexity in the soil and vegetation models. Here the near-surface water vapor moisture gradient is modulated by the fractional soil moisture M . Utilizing these scales the surface fluxes of heat and moisture are defined as in (5) and (6).

$$u_* = \frac{kU_z}{\ln\left(\frac{z}{z_{0m}}\right) - \psi_M\left(\frac{z}{L}\right) + \psi_M\left(\frac{z_{0m}}{L}\right)} \quad (2)$$

$$\theta_* = \frac{k(\theta_z - \theta_0)}{\ln\left(\frac{z}{z_{0h}}\right) - \psi_H\left(\frac{z}{L}\right) + \psi_H\left(\frac{z_{0h}}{L}\right)} \quad (3)$$

$$Q_* = \frac{k(q_z - q_{0s})M}{\ln\left(\frac{z}{z_{0h}}\right) - \psi_H\left(\frac{z}{L}\right) + \psi_H\left(\frac{z_{0h}}{L}\right)} \quad (4)$$

$$H = -\rho c_p \theta_* U_* \quad (5)$$

$$E = -\rho L_e Q_* U_* \quad (6)$$

The virtual heat flux combines these two fluxes as in (7). The primary stability parameter is given by the MOS length as defined in (8). For convective conditions another important characteristic scale is given by (9). Weber et al. (1982) provide a comprehensive survey of the MOS equations needed for this application with original references for all equations and we follow their approach in this discussion as well as in the LPM model. Discriminating between stable, neutral, and unstable conditions utilizes the ratio of height divided by the MOS length as in (10) plus the sign of the virtual heat flux H_v . These divisions plus the assignment of an appropriate depth for the planetary boundary layer (PBL) height are given by (11)-(13).

$$H_v = H + 0.61 \times 10^{-3} \bar{\theta} \rho^{-1} L_e^{-1} E \quad (7)$$

$$L = \frac{-\rho c_p \bar{\theta} u_*^3}{k g H_v} \quad (8)$$

$$w_* = \left(\frac{g H_v Z_i}{\rho c_p \bar{\theta}} \right)^{1/3} \quad (9)$$

$$\xi = \frac{z}{L} \quad (10)$$

$$Z_m = Z_i \quad \text{for } |\xi| \leq 0.05 \quad (11)$$

$$Z_m = Z_i \quad \text{for } |\xi| > 0.05 \text{ and } H_v > 0.0 \quad (12)$$

$$Z_m = \max(Z_i, h) \quad \text{for } |\xi| > 0.05 \text{ and } H_v \leq 0.0 \quad (13)$$

$$h = a \sqrt{\frac{u_* L}{f}} \quad (14)$$

The PBL height is used in all cases except for the stable case as described in (13) where the greater of the model PBL height and the scale height of the stable PBL is used where the latter is defined by (14).

3.1.3 Formulations for the stable case

Weber et al. (1982) give (15)-(18) as the formulations for the standard deviations and the Lagrangian time scales corresponding to each of the wind components for the stable situation. They are functions of the height, the PBL height, and the MOS velocity scale.

$$\sigma_u = 2u_* \left(1 - \frac{z}{Z_m}\right) \quad (15)$$

$$\sigma_v = \sigma_w = 1.3u_* \left(1 - \frac{z}{Z_m}\right) \quad (16)$$

$$T_u = 0.15 (z Z_m)^{0.5} \sigma_u^{-1} \quad (17)$$

$$T_v = 0.07 (z Z_m)^{0.5} \sigma_v^{-1} \quad (18)$$

$$T_w = 0.10 z^{0.8} Z_m^{0.2} \sigma_w^{-1} \quad (19)$$

3.1.4 Formulations for the Neutral Case

Weber et al. (1982) give (20)-(22) as the formulations for the standard deviations and the Lagrangian time scales corresponding to each of the wind components for the neutral case. They are functions of the height, the Coriolis parameter, and the MOS velocity scale.

$$\sigma_u = 2u_* \exp\left(\frac{-1.5fz}{u_*}\right) \quad (20)$$

$$\sigma_v = \sigma_w = 1.3u_* \exp\left(\frac{-1.0fZ}{u_*}\right) \quad (21)$$

$$T_u = T_v = T_w = \frac{0.5z}{\sigma_w (1 - 15fz)} \quad (22)$$

3.1.5 Formulations for the Unstable Case

Weber et al. (1982) give (23)-(30) as the formulations for the standard deviations and the Lagrangian time scales corresponding to each of the wind components for the unstable

case. In this category there are categories based on the fractional height with respect to the PBL depth. The independent variables for the deviations and time scales are the height, the PBL depth, the MOS velocity scale, the MOS length, the roughness length, and the free convection velocity scale.

$$\sigma_u = \sigma_v = u_* \left(12 - \frac{0.5Z_i}{L} \right)^{1/3} \quad (23)$$

$$\sigma_w = 0.96 w_* \left(\frac{3z}{Z_i} - \frac{L}{Z_i} \right)^{1/3}, \quad \text{for } \frac{z}{Z_i} < 0.03 \quad (24)$$

$$\sigma_w = w_* \min \left(0.96 w_* \left(\frac{3z}{Z_i} - \frac{L}{Z_i} \right)^{1/3}, 0.763 \left(\frac{z}{Z_i} \right)^{0.175} \right), \quad (25)$$

for $0.03 < \frac{z}{Z_i} < 0.4$

$$\sigma_w = 0.722 w_* \left(1 - \frac{z}{Z_i} \right)^{0.207}, \quad \text{for } 0.4 < \frac{z}{Z_i} < 0.96 \quad (26)$$

$$\sigma_w = 0.37 w_* \quad \text{for } 0.96 < \frac{z}{Z_i} < 1.0 \quad (27)$$

$$T_u = T_v = 0.15 Z_i \sigma_u^{-1} \quad (28)$$

$$T_w = \frac{0.10 \frac{z}{Z_i}}{0.55 + 0.38 \left(\frac{z - z_0}{L} \right)}, \quad \text{for } \frac{z}{Z_i} < 0.1 \text{ and } \frac{-(z - z_0)}{L} < 1.0 \quad (29)$$

$$T_w = \frac{0.15 Z_i \left(1 - \exp \left(-\frac{5z}{Z_i} \right) \right)}{\sigma_w}, \quad \text{for } \frac{z}{Z_i} > 0.1 \quad (30)$$

3.1.6 Formulations for the Lagrangian Autocorrelation Functions

The Lagrangian autocorrelation functions are modeled as an exponential decay as in (31)-(33) using the respective Lagrangian time scales as described above for each stability regime and the trajectory calculation time step Δt_s which for our calculations is set at 30 s.

$$R_u = \exp \left(\frac{-\Delta t_s}{T_u} \right) \quad (31)$$

$$R_v = \exp \left(\frac{-\Delta t_s}{T_v} \right) \quad (32)$$

$$R_w = \exp \left(\frac{-\Delta t_s}{T_w} \right) \quad (33)$$

3.1.7 Formulations for the Parameterized Turbulent Velocity Components

Equations 34-36 give the parameterized turbulent velocity components at a given time “t” as a function of the previous values Δt_s seconds back in time multiplied by the respective autocorrelation function. The random components of the turbulence are given by (37)-(39) and include a normal random deviate “r” which has a mean of zero and a standard deviation of one. An additional component for the vertical velocity is given by the drift velocity as in (40) and among other purposes restricts the number of particles that escape the PBL. The total wind components are then given by (41)-(43) and are the sum of the grid-scale mean and turbulent components.

One subtle issue is that the equations for the Lagrangian time scales and the standard deviations are actually in natural coordinates which means that the “u direction” is along the mean wind, and the “v direction” is perpendicular to the mean wind. The notation was not changed in order that it would be the same as those in the Weber et al. (1982) reference. In reality the parallel and perpendicular components are rotated to the u and v model wind component directions before they are used in the LPM.

$$u'(t) = u'(t - \Delta t_s) R_u \quad (34)$$

$$v'(t) = v'(t - \Delta t_s) R_v \quad (35)$$

$$w'(t) = w'(t - \Delta t_s) R_w \quad (36)$$

$$u'' = r \sigma_u \sqrt{(1 - R_u R_u)} \quad (37)$$

$$v'' = r \sigma_v \sqrt{(1 - R_v R_v)} \quad (38)$$

$$w'' = r \sigma_w \sqrt{(1 - R_w R_w)} \quad (39)$$

$$w'_d = 2T_w \sigma_w \frac{\partial \sigma_w}{\partial z} (1 - R_w) \quad (40)$$

$$u_t = u + u' + u'' \quad (41)$$

$$v_t = v + v' + v'' \quad (42)$$

$$w_t = w + w' + w'' + w'_d \quad (43)$$

3.1.8 Approach Used Above the PBL

The approach described in sections 3.1-3.5 is only applicable for the PBL. The approach to use for regions above the PBL is less well defined. Here we take the approach of utilizing some of the definitions found in the level 2 model in Mellor and Yamada (1974) along with the definitions of the Eulerian time scale and the ratio of the Lagrangian to the Eulerian time scale (β). Utilizing the vertical shear of the horizontal wind in (44) one can define the gradient Richardson number as in (45). With the definition and limit imposed on a mixing length in (46) an eddy diffusivity is defined as in (47) where the background value K_0 was set to $0.5 \text{ m}^2 \text{ s}^{-1}$. The flux Richardson number can be derived from the gradient Richardson number as shown by (48) which in turn helps define the Mellor-Yamada stability functions in (49)-(51). With the eddy diffusivity as defined as in (47) along with the Mellor-Yamada stability function in

(51) yields the standard deviation for the wind components in (52) assuming isotropic turbulence. The standard deviation plus the total wind speed yields the ratio of the Lagrangian to the Eulerian time scale in (53). The latter ratio plus the definition of the Eulerian time scale in (54) finally yields the Lagrangian time scale as defined in (55).

$$S = \sqrt{\frac{\partial u}{\partial z} \frac{\partial u}{\partial z} + \frac{\partial v}{\partial z} \frac{\partial v}{\partial z}} \quad (44)$$

$$R_i = \frac{\frac{g}{\theta_v} \frac{\partial \theta_v}{\partial z}}{S^2} \quad (45)$$

$$l_m = kz, \quad z \leq 75 \text{ m} \quad (46)$$

$$K = S l_m l_m \frac{R_c - R_i}{R_c} + K_0 \quad (47)$$

$$R_f = 0.725 \left(R_i + 0.196 - \sqrt{R_i^2 - 0.316 R_i + 0.346} \right) \quad (48)$$

$$S_m = 9.045 \sqrt{|R_f|}, \quad \text{for } R_f \leq -2, \quad S_m \geq 1 \quad (49)$$

$$S_m = 1.0 - 5.57 R_f, \quad \text{for } R_f > -2, \quad S_m \geq 1 \quad (50)$$

$$S_{mb} = \left(\frac{S_m}{3.873 \sqrt{|1 - R_f|}} \right)^{2/3} \quad (51)$$

$$\sigma_u = \sigma_v = \sigma_w = \frac{K}{(l_m S_{mb} \sqrt{3})} \quad (52)$$

$$\beta = \frac{0.60 \sqrt{(u^* u + v^* v)}}{\sigma_{u,v,w}}, \quad \beta \leq 5 \quad (53)$$

$$T_{e,uvw} = \frac{0.16 * l_m}{\sqrt{(u^* u + v^* v)}} \quad (54)$$

$$T_{L,uvw} = \beta T_{e,uvw} \quad (55)$$

3.1.9 Trajectory Calculation Procedures.

The wind components used in the trajectory calculations are obtained by linear interpolation in space and time from the hourly MM5 model output obtained from TAMU which has horizontal resolutions of 32-, 12-, and 4-km and 43 pressure-sigma levels. The total wind component as defined in (41)-(43) for each trajectory segment is the sum of the grid-scale values from MM5 plus a sub-grid component as described in section 3.0. The positions of each trajectory particle are calculated every 30 seconds. For each 30-second segment, calculations are done iteratively until the change in location from the previous iteration as a percentage of the total travel distance for the first iteration falls below a specified percentage. The wind components for each iteration of a given segment are the average of the values at the end of the previous segment plus the interpolated values in space and time of the new location at the prior iteration. The grid-

scale wind components are obtained at the new location for each iteration, but the turbulent components are held fixed at their values at the beginning of the trajectory segment. The mean total wind components along a trajectory segment are then given by (56)-(58) and the advection along the respective Cartesian coordinates is given by (59)-(61). Trajectories back in time are accomplished by setting the time step Δt_s to a negative value. This version of the LPM has an option that simulates a tetron by removing the influence of the vertical wind component. In this mode the vertical placement of the particle can be chosen as either a constant altitude above mean sea level from its initial launch time, or as a fixed altitude above local terrain during its travel. The web page address is <http://texaqs2.nsstc.uah.edu/> and the user name and password to the site are “tetron” and “rise”, respectively. More details on using the web page are underneath the “Instructions for Running Model” link on the home page.

$$\bar{u}_t^n = 0.50 \left(\begin{array}{l} u_t(t - \Delta t_s) + u(t)^n + u'(t - \Delta t_s) + \\ u''(t - \Delta t_s) \end{array} \right) \quad (56)$$

$$\bar{v}_t^n = 0.50 \left(\begin{array}{l} v_t(t - \Delta t_s) + v(t)^n + v'(t - \Delta t_s) + \\ v''(t - \Delta t_s) \end{array} \right) \quad (57)$$

$$\bar{w}_t^n = 0.50 \left(\begin{array}{l} w_t(t - \Delta t_s) + w(t)^n + w'(t - \Delta t_s) + \\ w''(t - \Delta t_s) + w_d'(t - \Delta t_s) \end{array} \right) \quad (58)$$

$$x^n(t) = x(t - \Delta t_s) + \bar{u}_t^n \Delta t_s \quad (59)$$

$$y^n(t) = y(t - \Delta t_s) + \bar{v}_t^n \Delta t_s \quad (60)$$

$$z^n(t) = z(t - \Delta t_s) + \bar{w}_t^n \Delta t_s \quad (61)$$

3.1.10 Plume Rise Calculation Procedures.

When a hot source is selected the Brigg’s plume rise approach is used to add an initial plume rise to the stack height to define an initial source height. Input stack parameters that are required are the stack temperature, velocity, and diameter.

Equations (62) and (63) define the Brigg’s buoyancy and momentum parameters, respectively. Selection of the appropriate plume rise equation depends upon the values of the buoyancy and momentum parameters, the difference between the stack and ambient air temperature in relation to a critical temperature difference threshold, and the atmospheric stability which is calculated by the average potential temperature lapse rate over the plume rise depth. The critical temperature thresholds for the unstable case for large and small values of the buoyancy parameter are given by (64) and (65). The critical temperature threshold for the stable case is given by (66). Equation (67) gives the plume rise for the unstable situation when the difference between the stack and ambient air temperature is less than the critical temperature difference threshold. Equation (68) gives the plume rise for the same situation except for the stable situation. For unstable situations when the difference between the stack and ambient air temperature is greater than the critical temperature difference threshold, the horizontal distance for final plume rise is required and is given by (69) and (70) according to the magnitude of the buoyancy

parameter. The plume rise for the unstable case for this situation is then given by (71). The final category to be considered is for the stable situation and for the case when the difference between the stack and ambient air temperature is greater than the critical temperature difference threshold. The plume rise for this situation is given by (72). When the stability is required for a calculation the relevant set of equations is solved iteratively until convergence is attained.

$$F_b = \frac{1}{4} g V_s D_s^2 \left(1 - \frac{T_a}{T_s} \right) \quad (62)$$

$$F_m = \frac{1}{4} V_s^2 D_s^2 \left(\frac{T_a}{T_s} \right) \quad (63)$$

$$\Delta T_c = 5.75 \times 10^{-3} T_s \frac{V_s^{2/3}}{D_s}, \quad \text{for } F_b \geq 55 \quad \text{and} \quad \frac{\partial \theta}{\partial z} \leq 0 \quad (64)$$

$$\Delta T_c = 2.97 \times 10^{-2} T_s \frac{V_s^{1/3}}{D_s}, \quad \text{for } F_b < 55 \quad \text{and} \quad \frac{\partial \theta}{\partial z} \leq 0 \quad (65)$$

$$\Delta T_c = 1.98 \times 10^{-2} T_s V_s \left(\frac{g}{T_a} \frac{\partial \theta}{\partial z} \right)^{1/2}, \quad \text{for } \frac{\partial \theta}{\partial z} > 0 \quad (66)$$

$$\Delta z_p = 3 \frac{D_s V_s}{W_s} \quad \text{for } T_s - T_a < \Delta T_c \quad \text{and} \quad \frac{\partial \theta}{\partial z} \leq 0 \quad (67)$$

$$\Delta z_p = 1.5 \left(\frac{F_m}{W_s \left(\frac{g}{T_a} \frac{\partial \theta}{\partial z} \right)^{1/2}} \right)^{1/3} \quad \text{for } T_s - T_a < \Delta T_c \quad \text{and} \quad \frac{\partial \theta}{\partial z} > 0 \quad (68)$$

$$\Delta x_f = 119 F_b^{2/5} \quad \text{for } T_s - T_a \geq \Delta T_c \quad \text{and} \quad \frac{\partial \theta}{\partial z} \leq 0 \quad \text{and} \quad F_b \geq 55 \quad (69)$$

$$\Delta x_f = 49 F_b^{5/8} \quad \text{for } T_s - T_a \geq \Delta T_c \quad \text{and} \quad \frac{\partial \theta}{\partial z} \leq 0 \quad \text{and} \quad F_b < 55 \quad (70)$$

$$\Delta z_p = 1.6 \frac{F_b^{1/3}}{\Delta x_f^{2/3}} \quad \text{for } T_s - T_a \geq \Delta T_c \quad \text{and} \quad \frac{\partial \theta}{\partial z} \leq 0 \quad (71)$$

$$\Delta z_p = 2.6 \left(\frac{F_b}{W_s \frac{g}{T_a} \frac{\partial \theta}{\partial z}} \right)^{1/3} \quad \text{for } T_s - T_a \geq \Delta T_c \quad \text{and} \quad \frac{\partial \theta}{\partial z} > 0 \quad (72)$$

3.2 Data transfer issues.

Figure 3.1 shows the main events that occur between Texas A&M (TAMU) and the web page at the University of Alabama (UAH). The system path begins at TAMU where for now the MM5 model will be run once daily for the 0000 UTC cycle. The UNIX cluster sasquatch.tamu.edu currently uses 16 nodes (32 processors) to integrate the MM5 model for the 36-, 12-, and 4-km grid system and finishes at about 1100 UTC for a 56-h simulation (personal communication, Gerry Creager, TAMU). Gerry has indicated that there are plans to add another 32 processors soon which should reduced the simulation time to 6 h or less.. Gerry Creager recently (~June 4-5) has succeeded in resolving the data transfer issues from TAMU to UAH. It will require on the order of a week to fully implement this data stream into the current web page application. The Unidata Local Data Manager (LDM) is being used to accomplish this transfer to the aqua.nsstc.uah.edu machine at UAH. Once data transfer begins program clpm.f90 on matrix.nsstc.uah.edu will continuously transform the MM5 data into the input files required for the LPM model. Program clpm.f90 includes calculating the Lagrangian time scales and standard deviations for each of the component wind directions and adds those variables to the original set of required MM5 variables. This is done to reduce the CPU requirements for the LPM since those variables have heavy exponential calculations. Program clpm.f90 outputs the data in a binary direct-access form (hereafter referred to as *idx files) that makes calculations easier within the LPM model. Once clpm.f90 has output an *idx file it is transferred to the ema.nsstc.uah.edu UNIX machine where the web interface, web graphics, and the LPM model are run.

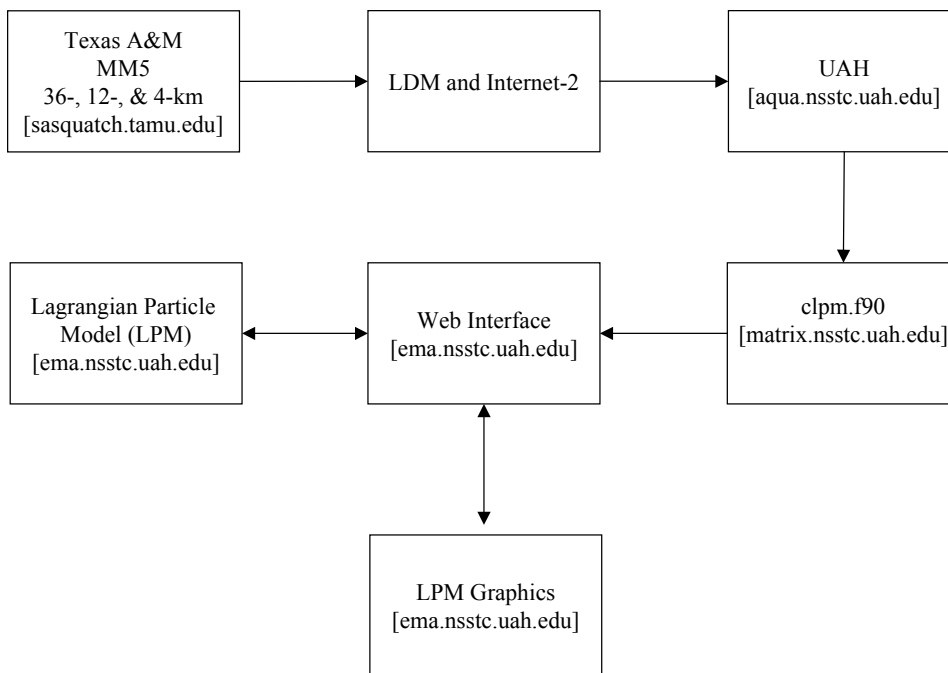


Figure 3.1 Schematic of data flow from Texas A&M University (TAMU) to the University of Alabama at Huntsville (UAH). Specific UNIX machines have their addresses in square brackets.

Table 1 Symbols of variables and constants used in this section with description and units.

Symbol	Description	Units
\overline{u}_t^n	Mean total wind in west-east direction along a trajectory segment at iteration “n” and time “t”	m s ⁻¹
\overline{v}_t^n	Mean total wind in north-south direction along a trajectory segment at iteration “n” and time “t”	m s ⁻¹
\overline{w}_t^n	Mean total wind in the vertical direction along a trajectory segment at iteration “n” and time “t”	m s ⁻¹
$x^n(t)$	West-east cartesian location at trajectory calculation iteration “n” and time “t”.	m
$y^n(t)$	North-south cartesian location at trajectory calculation iteration “n” and time “t”.	m
$z^n(t)$	Vertical location at trajectory calculation iteration “n” and time “t”.	m
$\frac{\partial \theta}{\partial z}$	Average vertical gradient in potential temperature over plume rise depth.	K m ⁻¹
$\overline{\theta}$	Mean surface layer potential temperature.	K
ρ	Surface layer density.	g kg ⁻¹
ξ	Ratio of z/L.	dimensionless
β	Ratio of Lagrangian to Eulerian timescales	dimensionless
Θ_*	Monin-Obukhov temperature scale.	K
Ψ_h	Integrated similarity function for heat.	dimensionless
Ψ_m	Integrated similarity function for momentum.	dimensionless
Θ_0	Potential temperature at the surface.	K
ΔT_c	Brigg’s critical stack temperature difference threshold	K

Δt_s	Trajectory time step.	s
σ_u	Standard deviation of wind component u.	$m s^{-1}$
Θ_v	Virtual potential temperature.	
σ_v	Standard deviation of wind component v.	$m s^{-1}$
σ_w	Standard deviation of vertical wind component w.	$m s^{-1}$
Δx_f	Brigg's horizontal distance for final plume rise.	,
Θ_z	Potential temperature at height z.	K
Δz_p	Brigg's stack plume rise.	m
a	Constant in equation for h.	dimensionless
c_p	Specific heat for dry air.	$J kg K^{-1}$
D_s	Stack diameter.	m
E	Moisture flux.	$W m^{-2}$
f	Coriolis parameter.	dimensionless
F_b	Brigg's stack buoyancy parameter.	$m^3 s^{-3}$
F_m	Brigg's stack momentum parameter.	$m^4 s^{-2}$
g	Acceleration of gravity	$m s^{-2}$
H	Heat flux.	$W m^{-2}$
h	Scale height of the stable boundary layer height.	m
H_v	Virtual heat flux.	$W m^{-2}$
k	Von Karmen constant	dimensionless
K	Eddy diffusivity	$m^2 s^{-1}$
K_0	Minimum Background Eddy diffusivity	$m^2 s^{-1}$
L	Monin-Obukhov similarity length.	m
L_e	Latent heat of condensation	$J g^{-1}$
l_m	Mixing Length	m
M	Moisture availability.	Fraction 0-1.0
Q^*	Monin-Obukhov water vapor scale.	$g kg^{-1}$
q_{0s}	Saturation mixing ratio at the surface corresponding to the temperature related to Θ_0 .	$g kg^{-1}$
q_z	Mixing ratio at height z.	$g kg^{-1}$
r	Random normal deviate with mean of zero and a standard deviation of one.	dimensionless
R_c	Critical Richardson Number	dimensionless
R_f	Gradient Richardson Number	dimensionless
R_i	Bulk Richardson Number	dimensionless
R_u	Lagrangian autocorrelation function in the u direction.	dimensionless
R_v	Lagrangian autocorrelation function in the v direction.	dimensionless
R_w	Lagrangian autocorrelation function in the vertical direction.	dimensionless
S	Total vertical shear of the horizontal wind.	s^{-1}
S_m	Mellor and Yamada Level 2 stability function for momentum.	dimensionless
S_{mb}	Mellor and Yamada Level 2 stability function for momentum.	dimensionless
t	time	s
T_a	Ambient air temperature at stack height.	K
T_e	Eulerian timescale	s

T_L	Lagrangian timescale	s
T_s	Stack temperature.	K
T_u	Lagrangian time scale in the u direction.	s
T_v	Lagrangian time scale in the v direction	s
T_w	Lagrangian time scale in the vertical direction.	s
u	Grid-scale mean wind component in the west-east direction.	$m s^{-1}$
u^*	Monin-Obukhov velocity scale or friction velocity.	$m s^{-1}$
u'	Parameterized turbulent velocity component in the u direction.	$m s^{-1}$
u''	Random component of the turbulent velocity component in the u direction.	$m s^{-1}$
u_t	Total wind component in the u direction including the grid-scale mean and the turbulent components.	$m s^{-1}$
U_z	Wind speed at height z.	$m s^{-1}$
v	Grid-scale mean wind component in the north-south direction.	$m s^{-1}$
v'	Parameterized turbulent velocity component in the v direction.	$m s^{-1}$
v''	Random component of the turbulent velocity component in the v direction.	$m s^{-1}$
V_s	Stack velocity.	$m s^{-1}$
v_t	Total wind component in the v direction including the grid-scale mean and the turbulent components.	$m s^{-1}$
w	Grid-scale mean wind component in the vertical direction.	$m s^{-1}$
w^*	Monin-Obukhov convective velocity scale.	$m s^{-1}$
w'	Parameterized turbulent velocity component in the vertical direction	$m s^{-1}$
w''	Random component of the turbulent velocity component in the vertical direction.	$m s^{-1}$
w'_d	Parameterized drift component of the turbulent velocity component in the vertical direction	$m s^{-1}$
W_s	Ambient wind speed at stack height.	$m s^{-1}$
w_t	Total wind component in the vertical direction including the grid-scale mean and the turbulent components.	$m s^{-1}$
z	Z is the height in meters above the surface.	m
Z_i	Height of planetary boundary layer.	m
Z_m	Chosen scale for height of planetary boundary layer.	
Z_{oh}	Roughness length for heat.	m
Z_{om}	Roughness length for momentum.	m

3.3 Model Benefits for Field Studies

The UAH LPM (McNider et al., 1988) has proved to be a useful tool for visualizing the transport and dispersion of atmospheric emissions. Since the model uses particles only as massless tracers, it is equally applicable to either gaseous or fine particulate emissions. When used in conjunction with mesoscale-model forecasts during field studies, it can assist scientists in formulating flight plans or deciding where portable monitors should be

located to optimize data collection. When used in retrospective analyses of field study data, it can help to determine whether plumes intersected aircraft flight paths or passed over fixed monitor locations.

3.4 Features of the Web-Based Version

We begin by describing the features of the current web version developed for TCEQ. Then we discuss features we would like to add for the upcoming field studies.

3.4.1. Current Features

Time series of mean meteorological fields are provided to LPM by the MM5 mesoscale model (Grell et al., 1994). The TCEQ version of LPM has access to only one model run. The output is available in a coarse, intermediate, or fine grid. The run was carried out by John Nielsen-Gammon for the period August 23 - September 2, 2000. Up to four source locations and corresponding emission rates can be specified. The sources may be either buoyant or non-buoyant sources. A plume-rise algorithm is included to handle buoyant emissions. The sources may be at the surface or elevated. Other locations of interest, representing monitor sites, for example, may be specified. These show up as color-coded markers in the output images.

Output consists of a series of snapshots of particle positions within the model domain. The snapshots view the model domain from overhead so that horizontal dispersion can be seen. A time series of such snapshots can be animated. During the TexAQS 2000 study UAH created animations of overhead views of the positions of particles emitted from several cities in Texas and other places in the Southeast and made them available for viewing by onsite scientists. Figure 1 is a frame taken from one of these animations.

3.4.2. Features Planned for the Upgraded Version

For the upgraded version we plan to give the user more choices of periods for which the model can be run and more flexibility in how the meteorological data can be used. We hope to be able to have access to twice-daily MM5 runs that have assimilated observations of wind profiler measurements in the Houston vicinity. The most recent runs should include a forecast period looking 24 hours or more into the future. After each run is made, it will be archived but could be accessed by users who want to study earlier periods.

We plan to use mouse clicks to identify source locations rather than prompting users to type in latitudes and longitudes. We also plan for users to choose whether the model should compute forward or backward trajectories from the selected sources.

We are presently assessing the extent to which we can include the Space Time Toolkit (STT) as part of the web package. The STT is a highly flexible, interactive graphics package developed at UAH that would allow users to simultaneously view multiple data sets (including the LPM output) in three dimensions. The tool aligns the data sets in space and time and allows the user to rotate, translate, and scale the region of view at will. The tool also permits the surface to be overlaid with state and county boundaries,

land-use images, and other such data sets that would assist in interpreting the results. The primary technical obstacle is moving STT from a work-station environment to the web.

4. TASK 3: Field Program Planning

Under task 3 of this project UAH participated in planning, operations and support of TexAQS II field campaigns. UAH participated in the phone conferences and meetings regarding the planning activities for TexAQSII. Under this activity UAH/SEAM began to formulate observational and analysis procedures to better quantify and understand the role of stationary fronts in producing extreme concentrations (appendix A). Under a previous HARC project through Texas A&M. an analysis was made of extreme events in the DFW region where stationary fronts were present. Under the present project we began to use EDAS analyses provided by TAMU to evaluate the characteristics of the wind fields and to begin to form observational plans for aircraft campaign's to explore the frontal zones.

We also responded to the Pacific Northwest Laboratory (PNL) requests with respect to the proposed tetron campaign. The goal is to evaluate transport from Houston with the tetron as a target for aircraft to track to make Lagrangian chemistry measurements. A summary of this activity will be presented in the next section. The initial results were presented at the HARC Field Program Planning Meeting March 15-16.

As a follow up to the Conceptual Model of Extreme Ozone Concentrations in East Texas, McNider made a presentation to the field program planning committee in Houston. The presentation included a discussion of the vertical structure of fronts and possible trajectories. A strawman for an aircraft observation program was also presented.

Work continued on defining plans and scientific objectives for TEXAQS05-06. McNider also participated in the HARC SAC and TEXAQS planning during the meeting June 1-3. A presentation was giving on "dead zones" and potential aircraft plans for examining the structure of stationary fronts. Also, an analysis of trajectories in the vicinity of the fronts. After notification that 10hrs of flight time was being allocated to study stationary fronts under TEXAQS05, we began preparations to plan details of the flight. A meeting was held in Muscle Shoals to meet with TVA aircraft personnel to explain the science background of the flight. We also discussed instrumentation and strawman flight plans.

4.1 Lagrangian Multi-particle Simulation for interpretation of Tetron Releases

As part of the TEXAQS2005-2006 Pacific Northwest Laboratory has proposed a tetron campaign. One goal is to evaluate transport from Houston with the tetron as a target for aircraft to track to make Lagrangian chemistry measurements. Under this TERC activity UAH proposed to make simulations of tetron releases using mesoscale model

simulations from TEXAQS2000 and employing the Lagrangian particle model (McNider et al. 1988) described above. The following is only meant to be a brief discussion of techniques and initial results. A more complete report will be given after feedback from PNL and when the full set of experiments have been completed.

The Lagrangian particle model allows for multiple trajectories where many particles are advected with the mean grid scale wind and by turbulence connected to the boundary layer parameterization in MM5. Thus, the model should provide an estimate of the spread of material that evolves through shear in the mean wind and turbulence.

The tetroon on the other hand provides a single trajectory based on a constant altitude setting. Thus, the goal of this work is to use the multiple particle models to determine how accurately a single tetroon might provide estimate of parcel transport. Additionally, experiments can be designed to test whether multiple tetroon releases might better capture the spread of the plume.

As part of this activity PNL has requested a matrix of runs from the Lagrangian particle model. They requested a puff of particles be released at sites and then simulated tetroons at 200 m AGL and 0.75 PBL height. The list of experiments requested by PNL are listed below.

A set of simulated releases at the following locations for 0600 LST (sunrise), 1000 LST (mid-morning), 1400 LST (mid-afternoon) and 1800 LST (sunset), with releases at both a fixed altitude (~ 0.2 km AGL) and an altitude that is a function of the boundary layer at these times, ideally 0.75 z_i where z_i = the boundary layer height.

-95.23W, +29.713N:

These are the (approximate) coordinates of a major VOC source (>6000 tons/year) along the Houston Ship Channel..

-95.40W, 30.35N

These are the coordinates of the Montgomery County Airport

Based on a review of the MM5 output the best daytime southerly flow events relative to the Houston area occur during the period of August 25-28, 2000. We have chosen August 25, 2000 for an initial set of experiments. However, this case may not be the strong southerly event in which PNL is interested. The results of this initial case are discussed below. We intend to simulate more days after consultation with PNL and will provide a complete report on the tetroon simulations by the end of March.

The MM5 simulations used in this simulation were made by John Nielsen-Gammon of TAMU and were based on the 12-km grid. In these initial set of experiments the tetroon trajectory calculations are accomplished by always keeping the tetroon a fixed distance above the local terrain. The first simulation was for a tetroon release at a fixed height of 200 m AGL. It was transported in a Lagrangian fashion using the interpolated winds from MM5. Figure 2-3 show the tetroon indicated by a "B" compared to a burst of particles released at 200 m. Both the particle and balloon release were made at 23 UTC (late

afternoon). It can be seen that the balloon tracks well the material that is close to the ground but there is substantial deformation of the puff overnight.

Figures 4-5 show a similar simulation except that the balloon is released at 2000 m (near the top of the boundary layer) and the release time is early morning (11 UTC). It can be seen that the higher release tracks the path of the particles in the upper part of the boundary layer.

Figure 6-7 shows depictions of a continuous release at two times. This can be used to put the tagged puffs in perspective. Finally figures 7-8 show a snapshot of the MM5 winds which are being used to transport the balloon and the particles.

4.2 Interpretation of Role of Inhomogeneous Wind Fields

The following provides documentation of thought experiments relative to the role of regions of light winds such as dead zones near stationary fronts or stalled sea breezes. The first approach (section 4.2.1) is to view concentrations from a Eulerian point of view. The Eulerian analyses show that for a steady spatially homogeneous emission rate concentrations are primarily controlled by boundary conditions not by variations in surface wind speeds. This is perhaps counter intuitive to the view that light winds alone would cause a variation in concentration alone with higher concentrations in regions of light winds.

The second approach views the concentrations from Lagrangian view. This view which is perhaps easier to interpret also shows that wind speed variations alone will not produce variations in concentrations for spatially homogeneous emissions. A second Lagrangian analysis clearly shows that wind speed variations coupled with non-homogeneous emissions will produce higher concentrations in regions of light winds.

4.2.1 Eulerian Analyses

Consider the advection equation for a pollutant of concentration C

$$\frac{\partial C}{\partial t} + u \frac{\partial C}{\partial x} + v \frac{\partial C}{\partial y} + w \frac{\partial C}{\partial z} = S, \quad (1)$$

where S represents pollution sources. We first apply the equation to an infinite line source, then to a finite line source of length $2L$. We superimpose a rectangular Cartesian coordinate system on the line. The second case, in which the center of the finite segment is taken to be the origin, is shown in Figure 4.1.

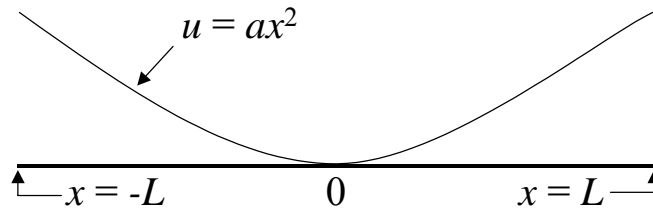


Figure 4.1. A finite line source emitting at a constant rate of Q units of mass per unit length per unit time is subjected to a variable wind that becomes zero at the origin. The wind profile shown increases quadratically with distance from the origin. See Section B.1 for a solution to this formulation of the problem.

For a line source, S is expressed as mass per unit length per unit time. We assume the emission rate to be constant and denote it by Q . If we also assume the wind flow is purely westerly and has no vertical motion, then (1) simplifies to

$$\frac{\partial C}{\partial t} + u \frac{\partial C}{\partial x} = Q. \quad (2)$$

We will further assume the magnitude of the flow to increase quadratically with distance from the origin. Two cases will be considered—the first, when the flow becomes zero at the origin:

$$u = ax^2, \quad a > 0. \quad (3)$$

In the second, the flow reaches a minimum at the origin but remains positive:

$$u = ax^2 + b, \quad a, b > 0. \quad (4)$$

A. Infinite Line Source

A.1. Stagnation at the Origin

Incorporating (3) into (2), we obtain

$$\frac{\partial C}{\partial t} + ax^2 \frac{\partial C}{\partial x} = Q. \quad (5)$$

Since the line is infinite, the boundary conditions take the form

$$\lim_{x \rightarrow -\infty} C = C_0 \quad (6)$$

and

$$\lim_{x \rightarrow \infty} C = C_1. \quad (7)$$

The concentration reaches a steady state that can be found by letting $\partial C/\partial t = 0$ in (5). Then (5) reduces to

$$\frac{\partial C}{\partial x} = \frac{Q}{ax^2}. \quad (8)$$

Before integrating (8) to obtain a solution, we note that it has a singularity and hence no solution at the origin. We should not be surprised to find different solutions on either side of the origin. Furthermore, we note that slopes of the solution curves are always positive and are identical at points equidistant from the origin. The general solution of (7) is

$$C = K - Q/ax, \quad (9)$$

where K is a constant of integration. Equation (9) indicates that as x approaches the origin from the west ($x < 0$), the concentration increases without bound. As x approaches from the east ($x > 0$), the concentration decreases without bound. Applying the boundary condition (6), we obtain the solution west of the origin.

$$C = C_0 - Q/ax. \quad (10)$$

Applying (7), we obtain the solution for the east.

$$C = C_1 - Q/ax. \quad (11)$$

The solution is displayed in Figure 4.2.

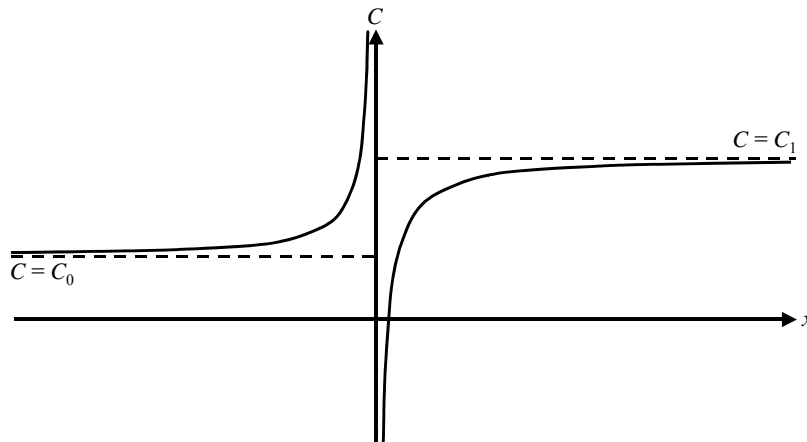


Figure 4.2. The solution curves for the infinite line source with uniform emission rate along the line. The asymptotes are determined by the concentrations approached as the distance from the origin increases without bound.

For the most part this solution appears to be physically consistent (although not physically realistic since wind speed cannot increase without bound). A quadratically increasing wind speed drives the concentration resulting from a linear emission rate toward zero so that in the limit only the background concentrations remain (C_0 in the west, and C_1 in the east). In the region $0 < x < Q/aC_1$, concentration is negative. This result runs counter to physical reality but is an artifact of the problem formulation.

A.2. Small, Positive Flow at the Origin

To avoid having a singularity at the origin we assume that the wind speed, although quadratic, does not reach zero at the origin. An example is shown in Figure 4.3.

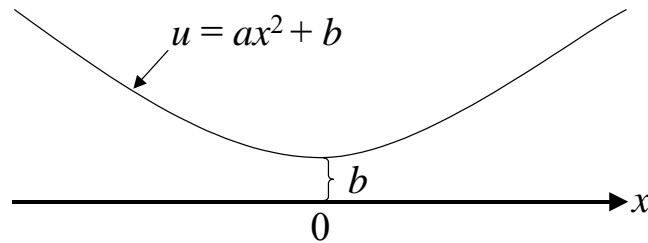


Figure 4.3. An infinite line source emitting at a constant rate of Q units of mass per unit length per unit time is subjected to a variable wind that becomes small and positive at the origin. The wind profile shown increases quadratically with distance from the origin. See Section A.2 for a solution to this formulation of the problem.

Thus, we assume u takes the form shown in (4). Substituting (4) into (2), we obtain

$$\frac{\partial C}{\partial t} + (ax^2 + b) \frac{\partial C}{\partial x} = Q. \quad (12)$$

and the steady-state problem is

$$\frac{\partial C}{\partial x} = \frac{Q}{(ax^2 + b)}. \quad (13)$$

The general solution at any point x on the line is

$$C = \frac{Q}{\sqrt{ab}} \arctan\left(\sqrt{\frac{a}{b}}x\right) + K, \quad (14)$$

where K is a constant of integration. If we apply boundary condition (6), we get

$$C = C_0 + \frac{Q}{\sqrt{ab}} \left(\arctan \left(\sqrt{\frac{a}{b}} x \right) + \frac{\pi}{2} \right) \quad (15)$$

as the solution. The solution for the case of $a=1$, $b=1$, $Q=1$, and $C_0=1$ is depicted in Figure 4.4.

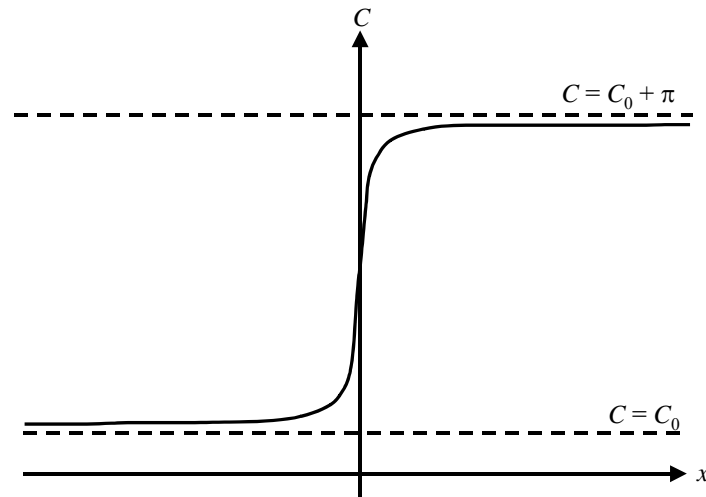


Figure 4.4. The solution curve for an infinite line source with uniform emission rate along the line. The quadratic wind speed reaches a positive minimum at $x=0$. The asymptotes are determined by the concentration approached as the westward distance from the origin increases without bound.

B. Finite Line Source

B.1. Stagnation at the Origin

For a finite line source the boundary conditions are

$$C(-L) = C_0 \quad (16)$$

and

$$C(L) = C_1. \quad (17)$$

For $x < 0$, the solution of (8) is

$$C = C_0 - \frac{Q}{a} \left(\frac{1}{L} + \frac{1}{x} \right) \quad (18)$$

For $x > 0$, the solution is

$$C = C_1 + \frac{Q}{a} \left(\frac{1}{L} - \frac{1}{x} \right) \quad (19)$$

B.2. Small, Positive Flow at the Origin

For a finite line source that does not stagnate at the origin the upwind boundary condition is

$$C(-L) = C_0 \quad (20)$$

The solution of (13) is

$$C = C_0 + \frac{Q}{\sqrt{ab}} \left[\arctan \left(\sqrt{\frac{a}{b}} x \right) + \arctan \left(\sqrt{\frac{a}{b}} L \right) \right] \quad (21)$$

Summary of Eulerian Analyses

Both of the source configurations show that wind speed variations alone cannot produce high concentrations in regions of light winds. Rather concentrations are governed by boundary conditions.

4.2.2 Lagrangian Analyses

While the above analytical thought models demonstrate that wind inhomogeneities alone cannot produce variations in concentrations for homogeneous emissions, while mathematically robust are not intuitively clear. An alternate approach is to examine the situation from a Lagrangian view.

Consider, two parcels moving in a Lagrangian manner –one in a higher wind regime than the other over a homogeneous emission region (see Figure 4.5). From a Lagrangian view the change in concentration is given by

$$\frac{dC}{dt} = Q \quad (22)$$

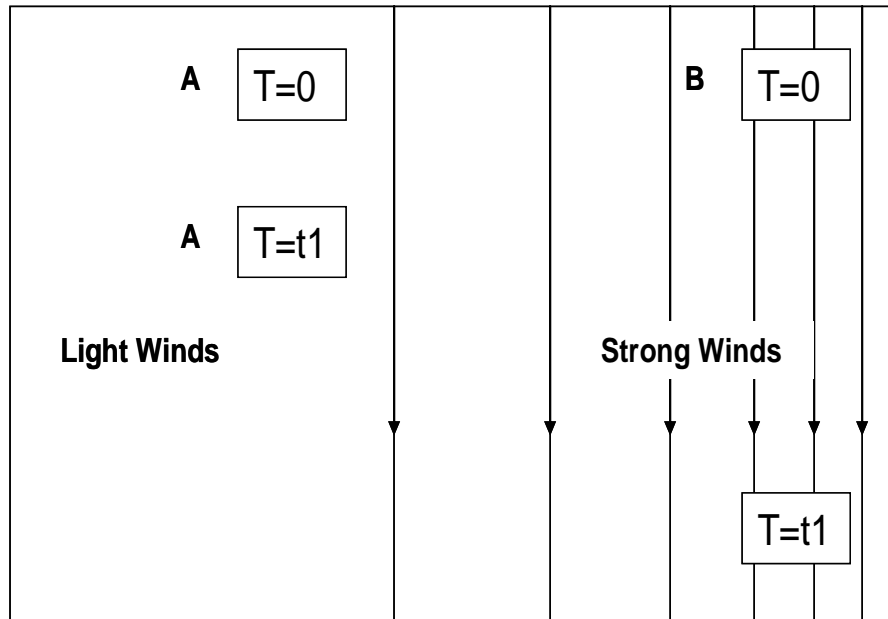


Figure 5. Schematic of Lagrangian parcels travel across a homogeneous emission field. Note that both parcels have the same concentration at time t_1 . Thus, all parcels would have same concentration at t_1 thus wind speed does not introduce inhomogeneities for homogeneous emissions.

For the homogeneous emission case from equation 22 the concentration for both parcels after time t_1 is

$$C = t_1 X Q + c_0$$

Thus, both parcels after a given time with the same starting concentrations are equal. Since these markers could be representative of all parcels we conclude that after time t_1 all concentrations are the same. Thus, wind inhomogeneities alone cannot produce inhomogeneous concentrations.

Next, consider a similar case except for an emission strip (see figure 4.6). Now we see that the concentrations are no longer equal in that the parcel in the light wind stays over the source region a longer time and thus has higher emissions.

Thus in summary we see that inhomogeneous wind fields in conjunction with inhomogeneous emissions can produce inhomogeneous concentrations.

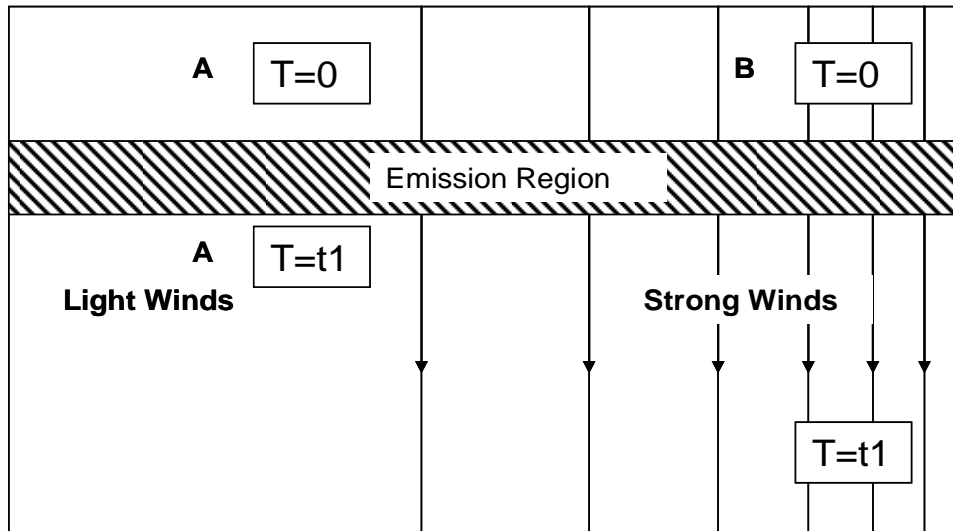


Figure 6. Schematic of Lagrangian parcels passing over emission region. Note parcel A at time $t1$ would have a larger concentration than parcel B since it would spend a longer period of time over the source region.

REFERENCES

- Chang, J.S., R.A. Brost, I.S.A. Isaksen, S. Madronich, P. Middleton, W.R. Stockwell, and C.J. Walcek, 1987: A three-dimensional eulerian acid deposition model: physical concepts and formulation, *J. Geophys. Res.*, **92 (D12)**: 14681-14700.
- EPA, 1999: Science Algorithms of the EPA Models-3 Community Multiscale Air Quality (CMAQ) Modeling System. EPA-600/R-99/030.
- Grell, G. A., J. Dudhia, and D. R. Stauffer, 1994: *A Description of the Fifth-Generation Penn State/NCAR Mesoscale Model (MM5)*. NCAR Technical Note NCAR/TN-398+STR, National Center for Atmospheric Research, Boulder, Colorado.
- Grell, G.A., J. Dudhia, and D.R. Stauffer, 1994: The Penn State/NCAR Mesoscale Model (MM5). NCAR Technical Note, NCAR/TN-398+STR, 138 pp.
- Hanna, S. R., 1979: Some statistics of Lagrangian and Eulerian wind fluctuations. *J. Appl. Meteor.*, **18**, 518-525.
- Madronich, S., 1987: Photodissociation in the atmosphere, 1, actinic flux and the effects of ground reflections and clouds. *Journal of Geophysical Research*, **92**, 9740-9752.
- McNider, R. T., M. D. Moran, and R. A. Pielke, (1988): Influence of diurnal and inertial boundary-layer oscillations on long-range transport. *Atmos. Environ.*, **22**, 2445-2462.
- Mellor, G. L. and T. Yamada, 1974: A hierarchy of turbulence closure models for planetary boundary layers. *J. Atmos. Sci.*, **31**, 1791-1806.
- NCAR (2003): MM5 Modeling System Version 3, NCAR website --- <http://www.mmm.ucar.edu/mm5/doc1.html>.
- Pielke, R. A., R. T. McNider, M. Segal, and Y. Mahrer, 1983: The use of a mesoscale numerical model for evaluations of pollutant transport and diffusion in coastal regions and over irregular terrain. *Bull. Amer. Meteor. Soc.*, **64**, 243-249.
- Smith, F. B., 1968: Conditioned particle motion in a homogeneous turbulent field. *Atmos. Environ.*, **2**, 491-508.
- Smith, F. B., 1968: Conditioned particle motion in a homogeneous turbulent field. *Atmos. Environ.*, **17**, 194-197.
- Weber, A. H., J. S. Irwin, W. B. Petersen, J. J. Mathis, Jr., and J. P. Kahler, 1982: Spectral scales in the atmospheric boundary layer. *J. Appl. Meteor.*, **21**, 1622-1632.

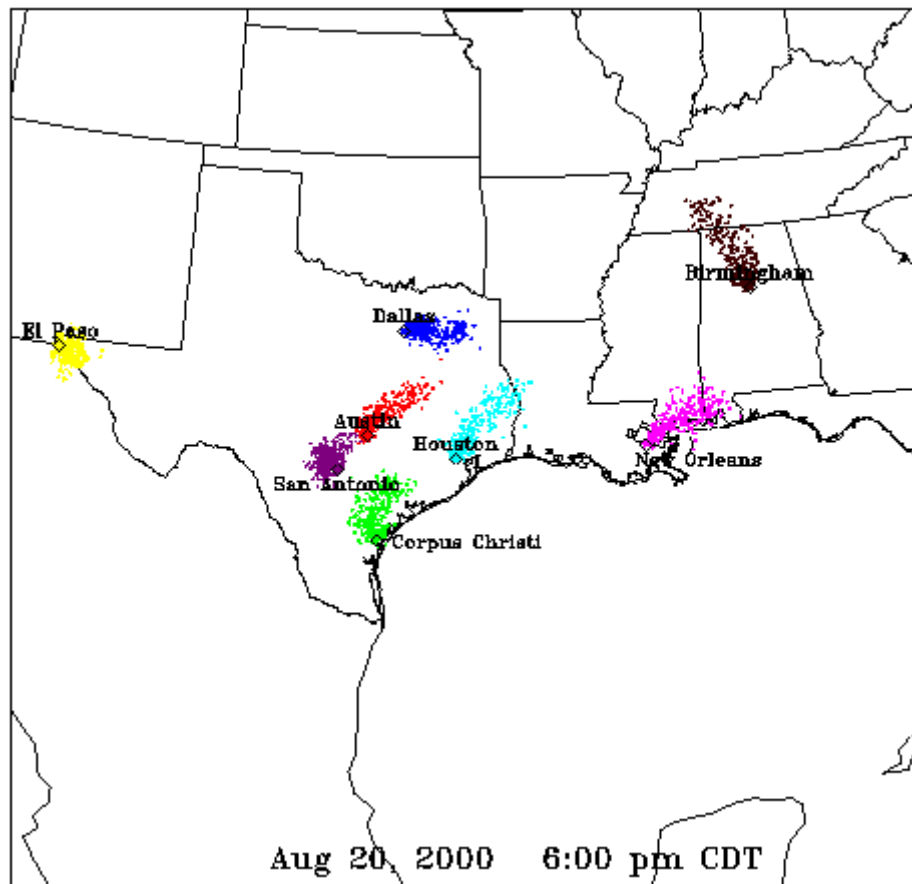
6. FIGURES:

Figure 1. A snapshot of particles released from five cities in Texas, Louisiana, and Alabama during the period of the TexAQS 2000 study. The particle positions are those calculated by LPM twelve hours after the first particle was released. Meteorological data for LPM was provided by NASA from its customized version of MM5, which is run twice each day in forecast mode.

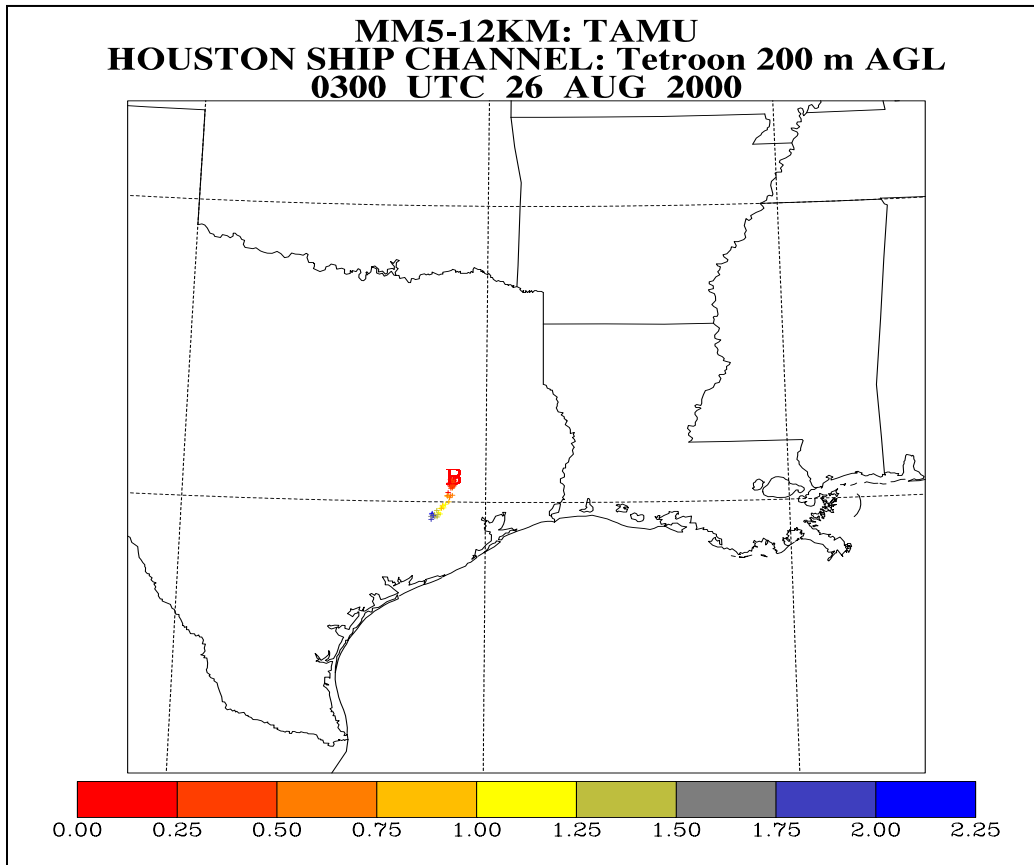


Figure 2. Tetroon “B” and particle puff after 3 hours of transport

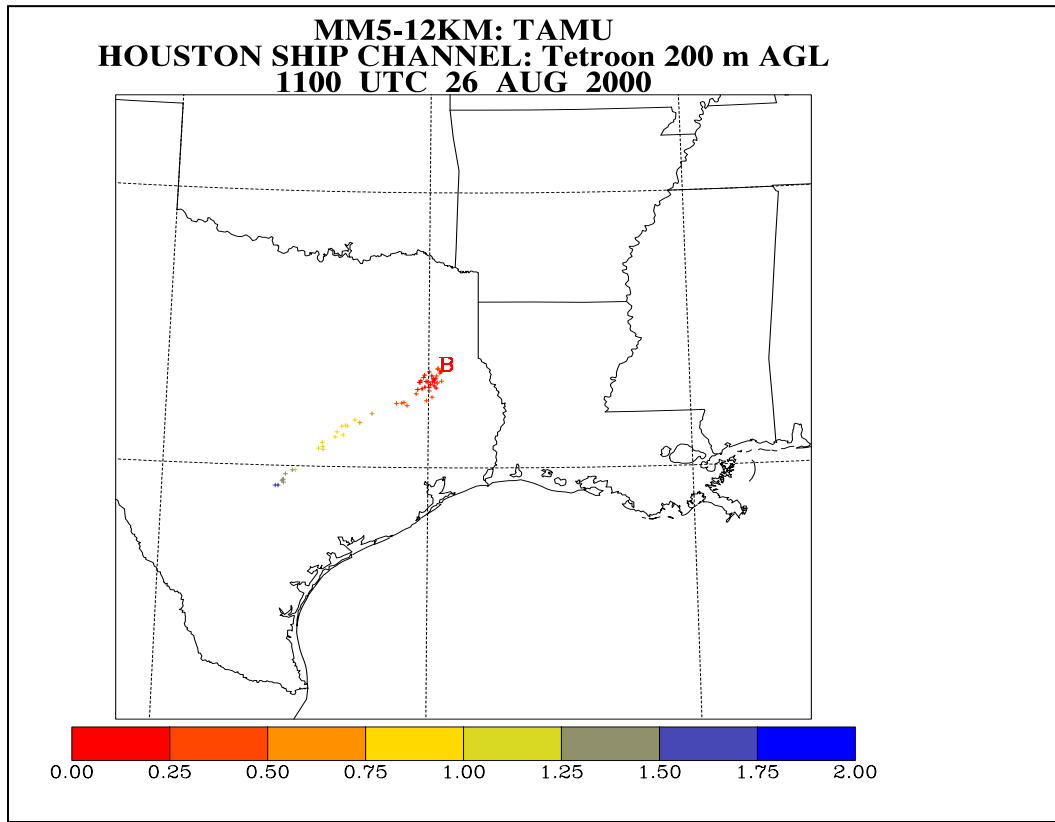


Figure 3. Same as figure 2 except after 11 hours of transport.

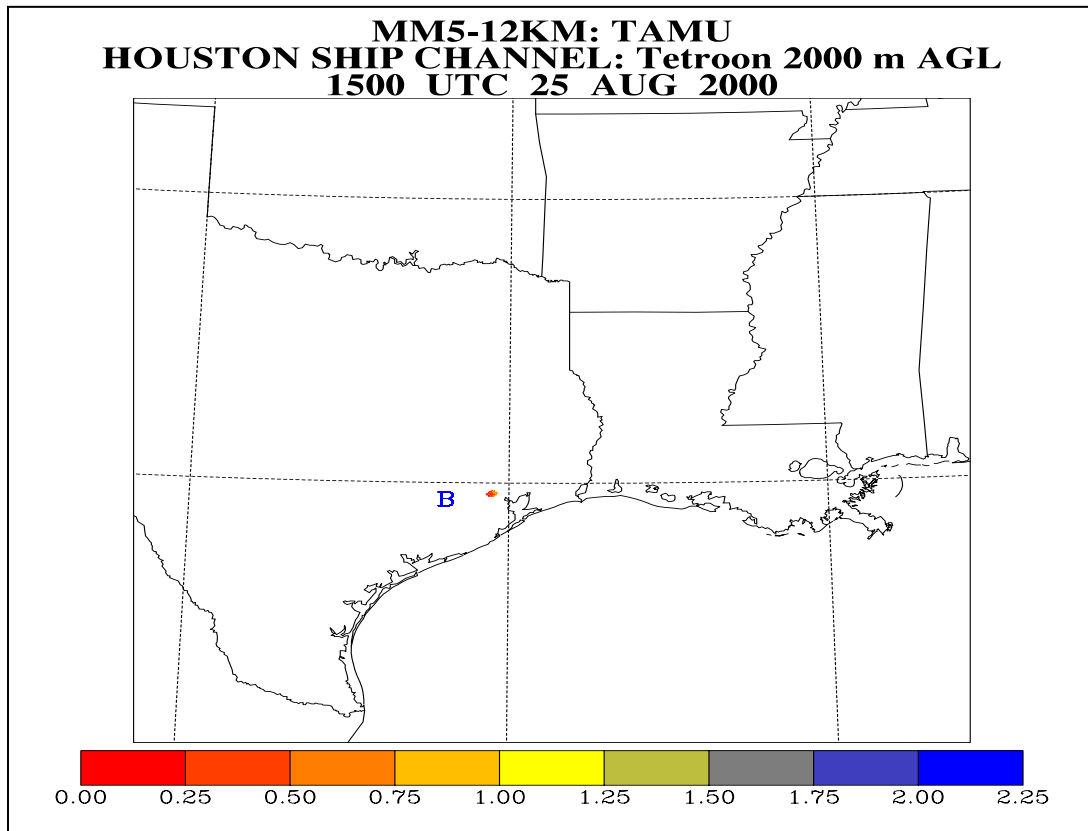


Figure 4. Tetroon “B” and particle puff after 3 hours of transport.
Tetroon is at 2000m AGL

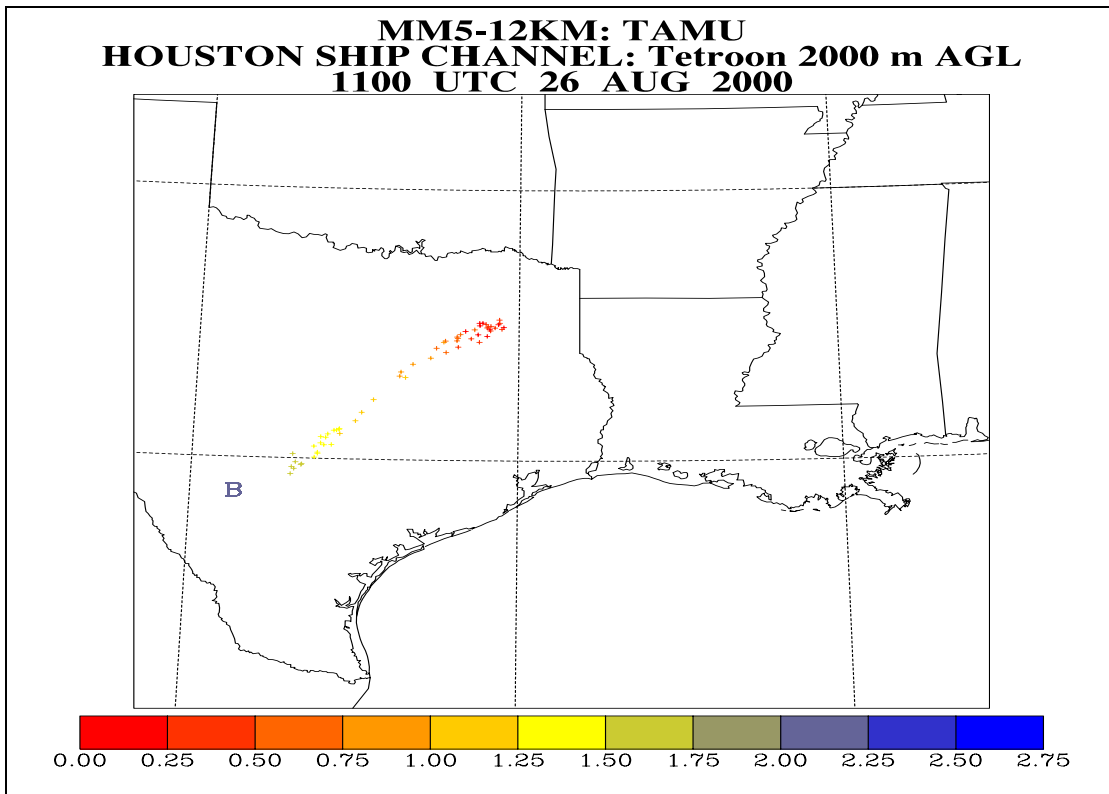


Figure 5. Same as figure 4 except after 23 hours of transport.

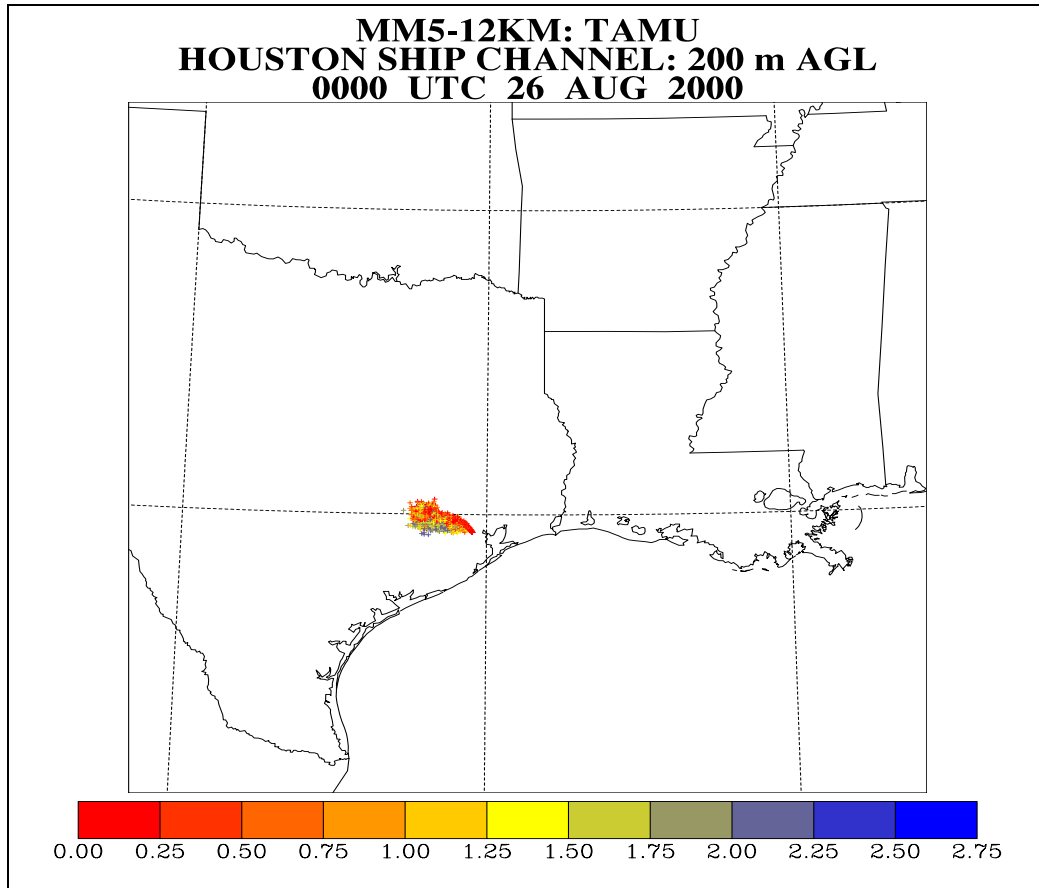


Figure 6. Depiction of the continuous plume after 12 hours of releases.

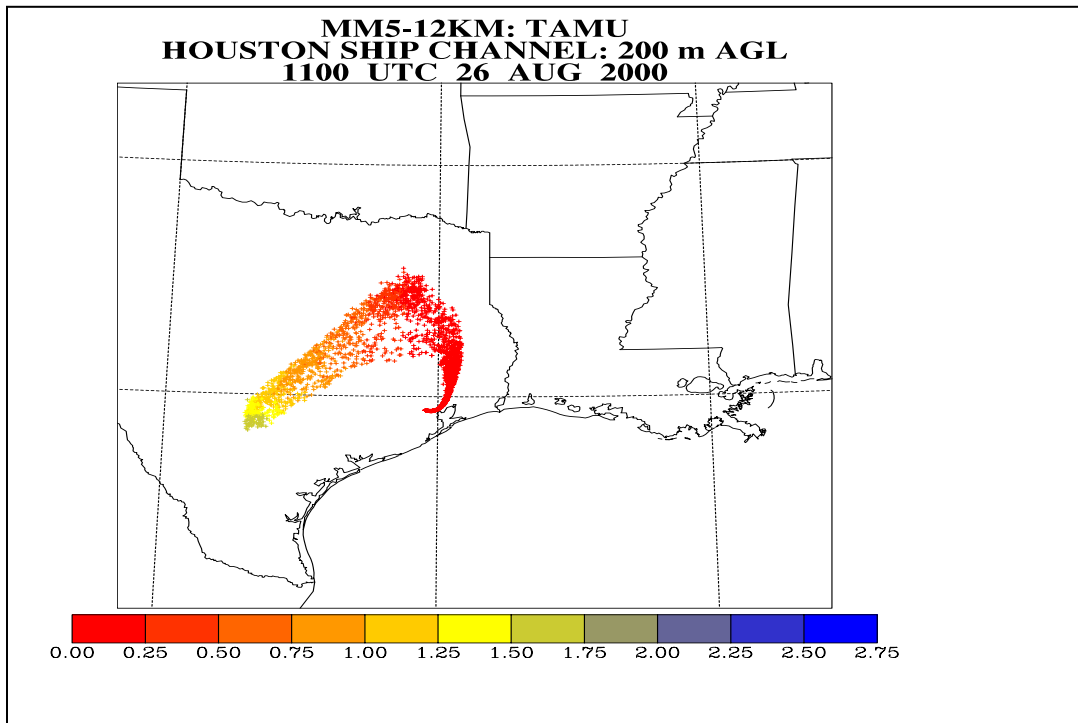


Figure 7. Continuous release after 23 hours.

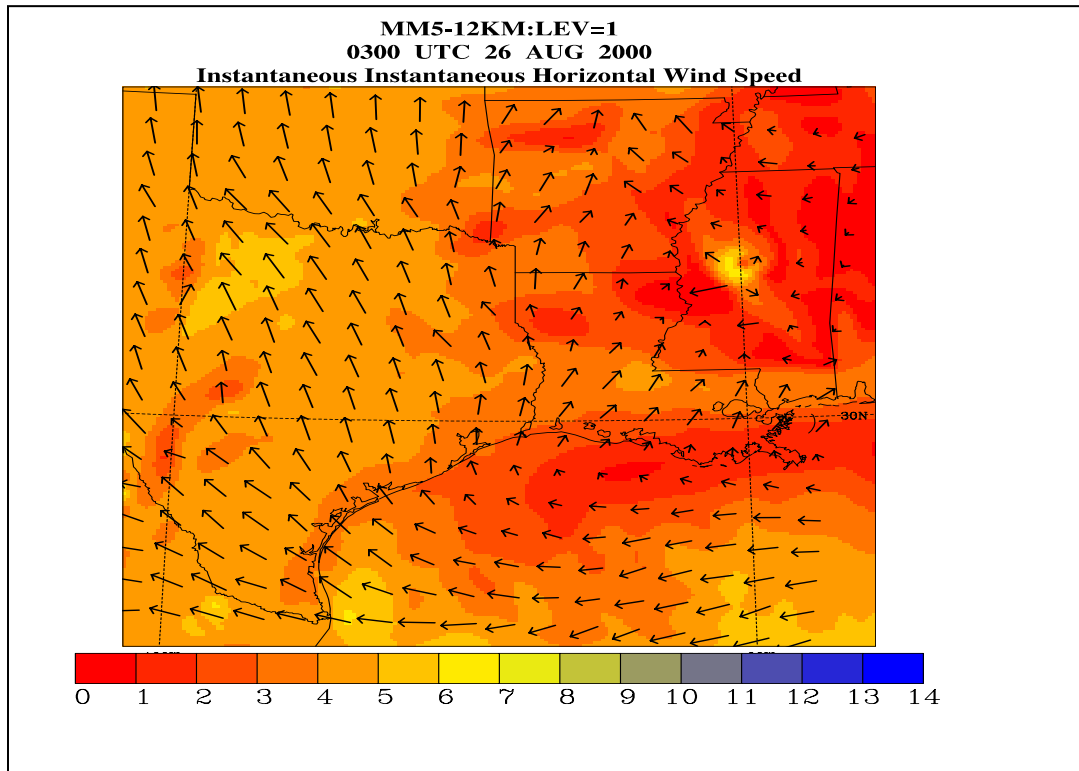


Figure 7. MM5 winds at level 1 (approximately 10 meters)

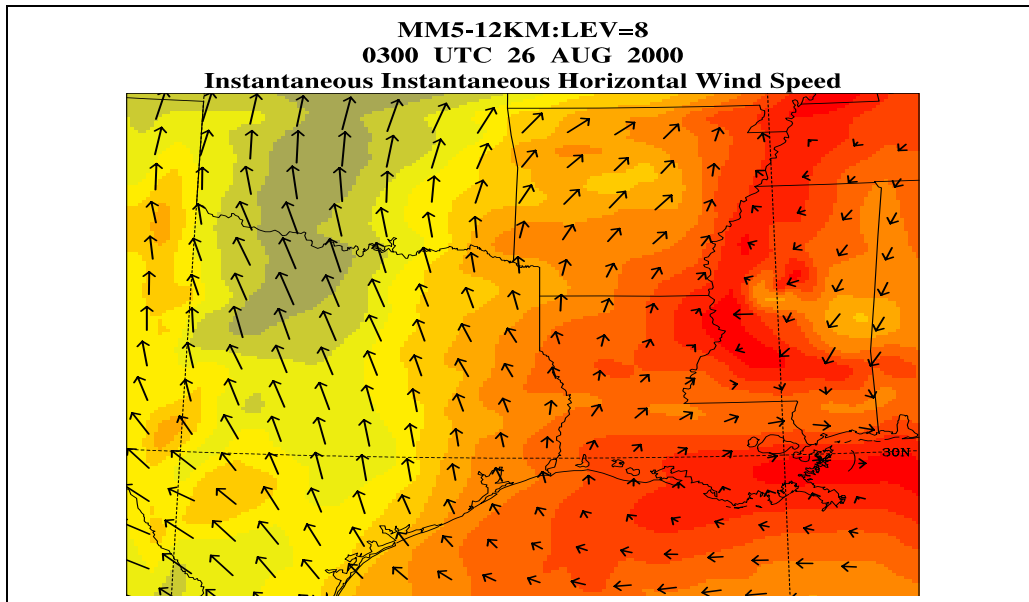


Figure 8. MM5 winds at level 8 (approximately 350m)

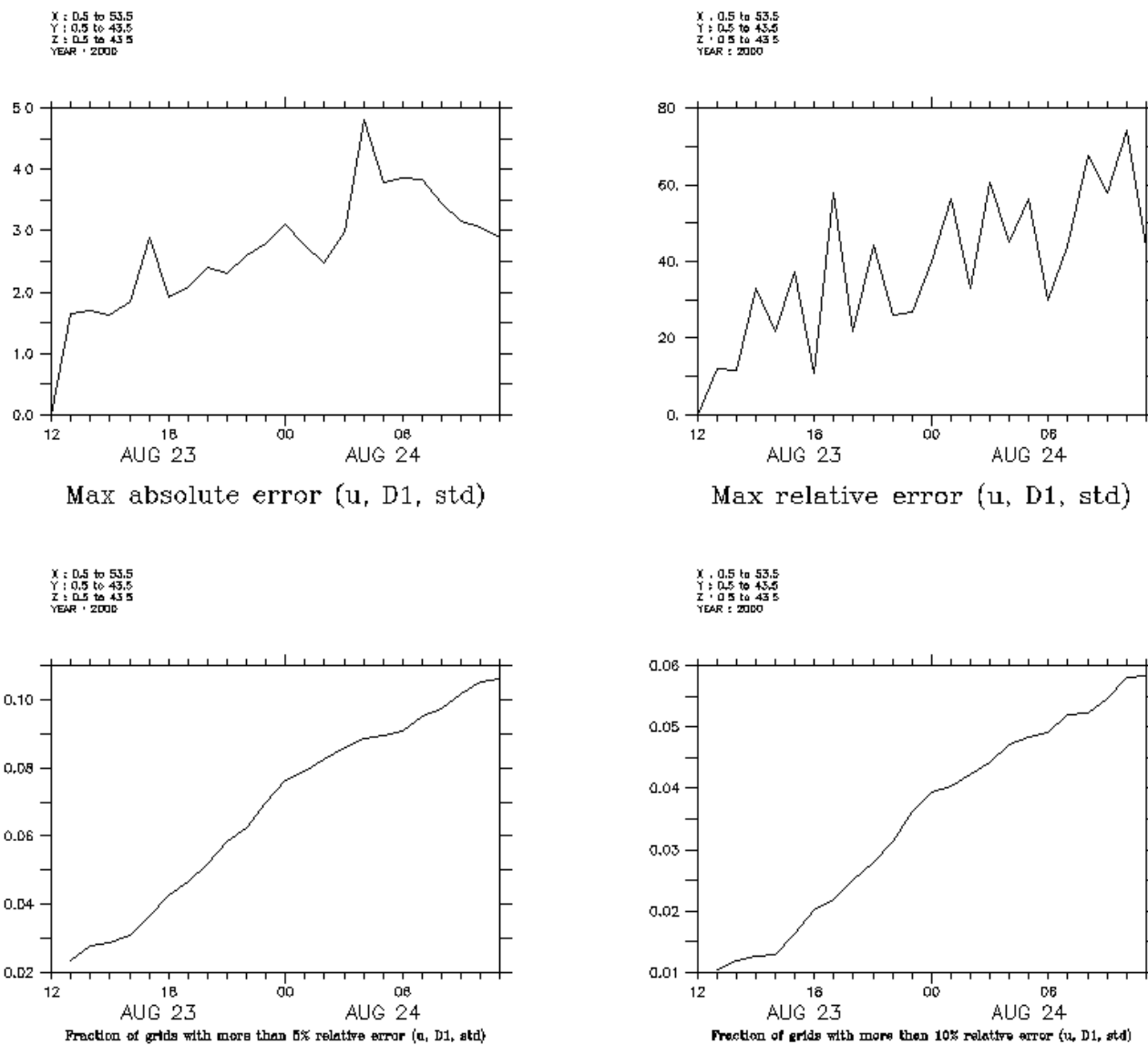


Figure 9. The difference in horizontal wind component (u) in m/s between a run using a single processor and one using MPP option of MM5 for domain 1. Standard MM5 version 3.72 was used for simulations. The panels show the maximums in absolute and relative errors as well as rapid propagation of error in the domain.

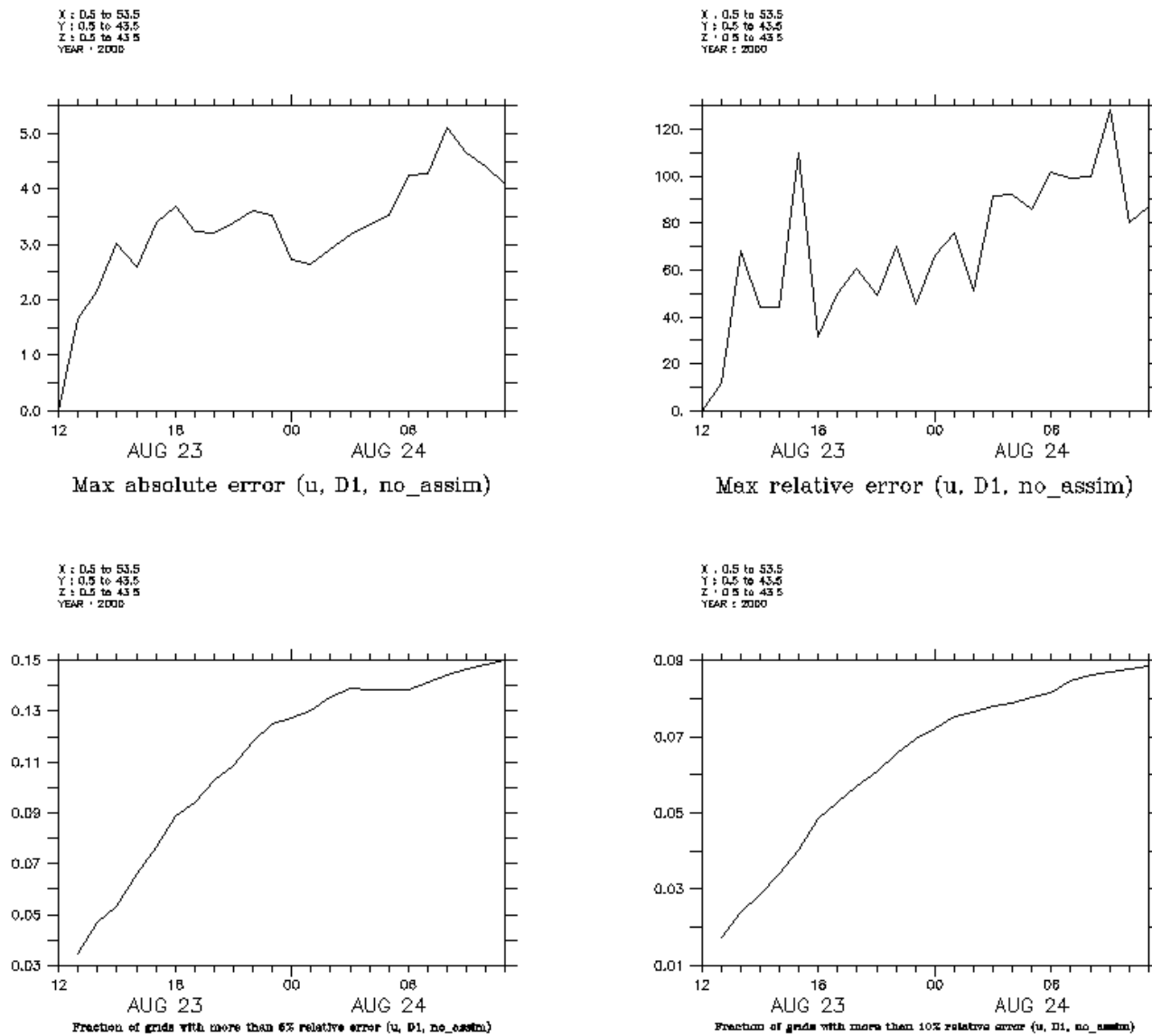


Figure 10. The difference in horizontal wind component (u) in m/s between a run using a single processor and one using MPP option of MM5 for domain 1 using MM5 version 3.72 that was modified for GOES data assimilation. No satellite assimilation was performed in this simulation. The panels show the maximums in absolute and relative errors as well as rapid propagation of error in the domain.

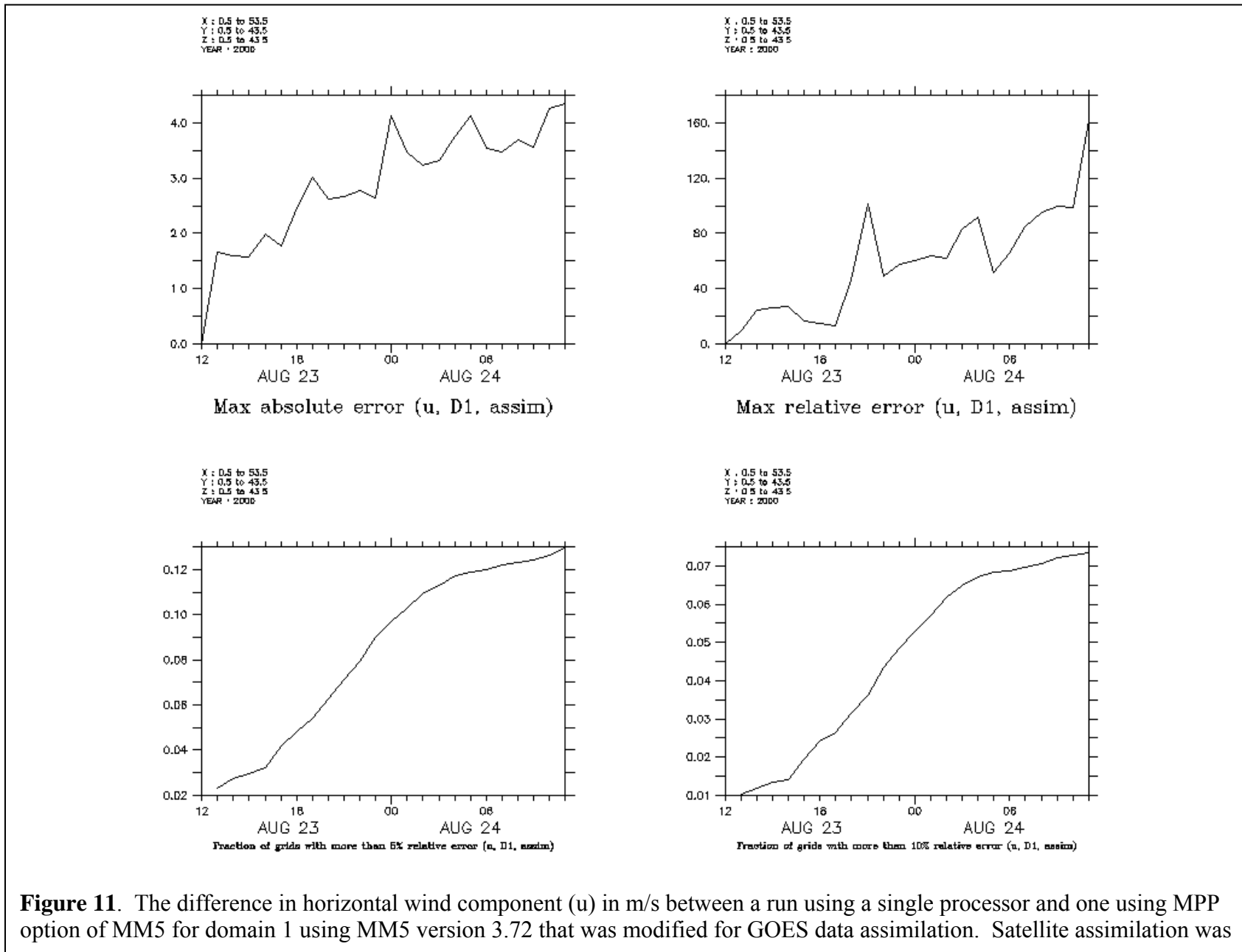
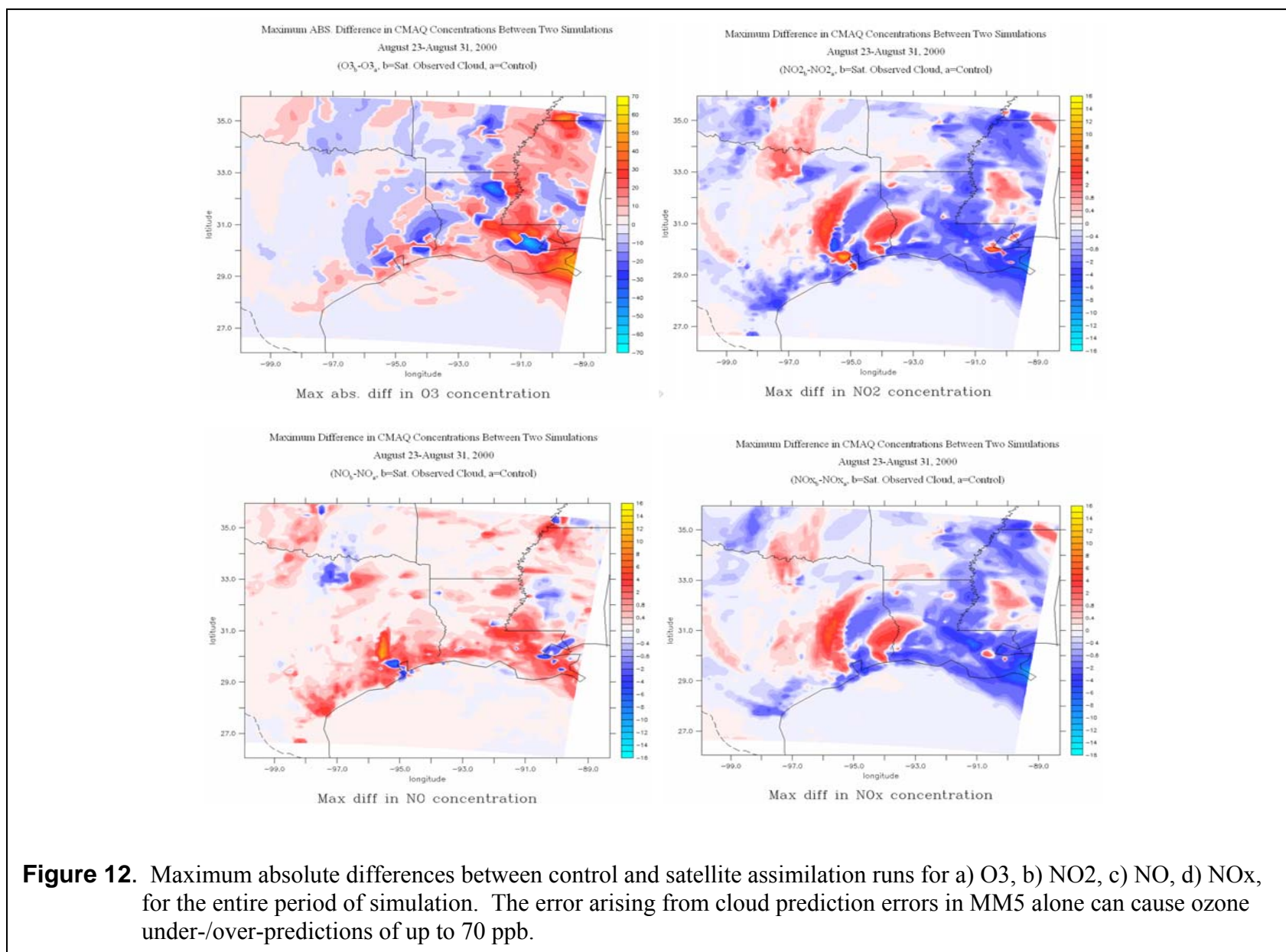


Figure 11. The difference in horizontal wind component (u) in m/s between a run using a single processor and one using MPP option of MM5 for domain 1 using MM5 version 3.72 that was modified for GOES data assimilation. Satellite assimilation was



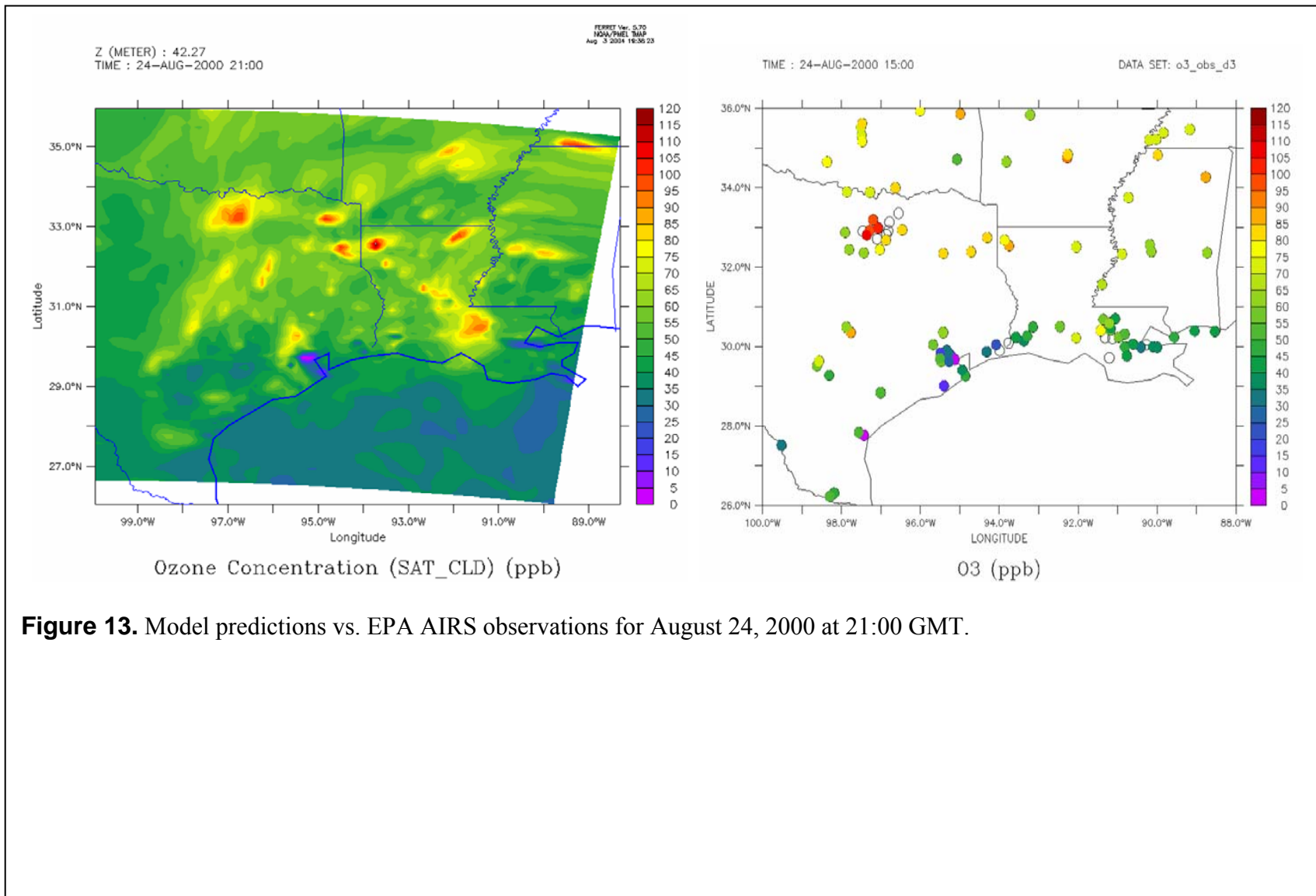


Figure 13. Model predictions vs. EPA AIRS observations for August 24, 2000 at 21:00 GMT.

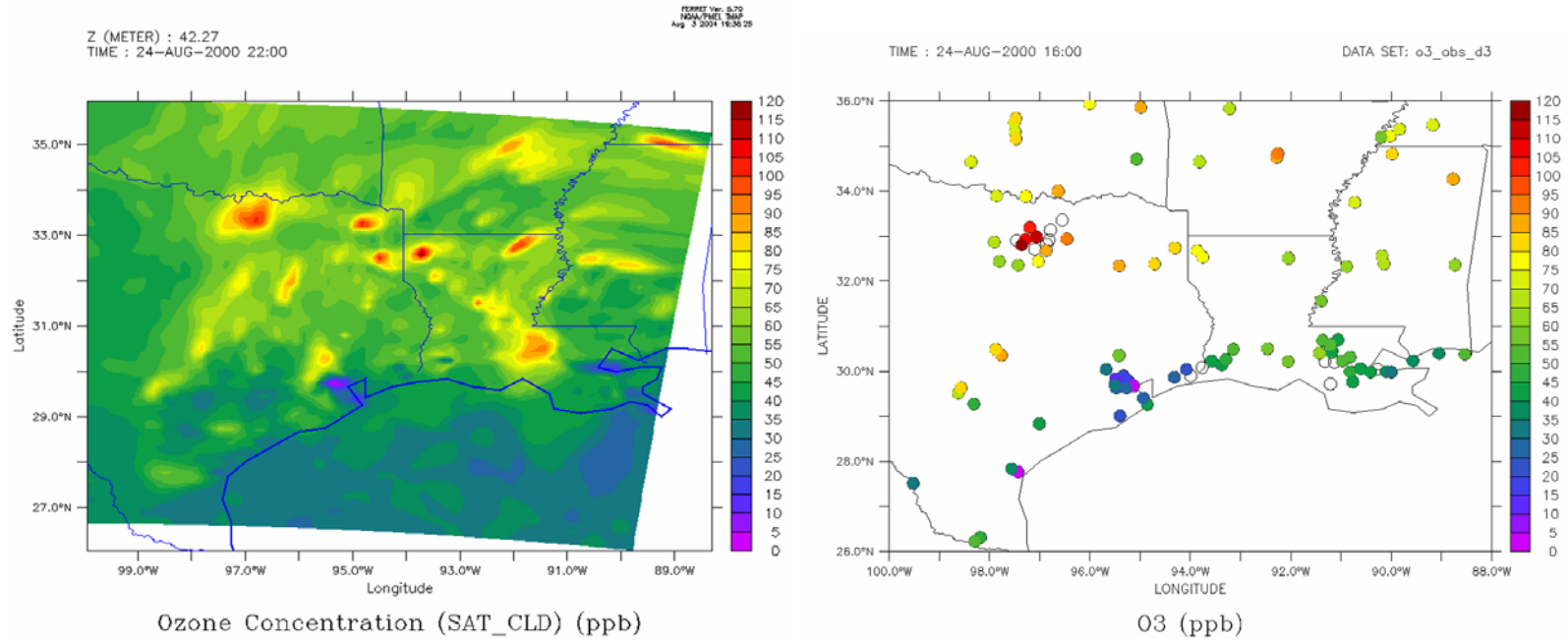


Figure 14. Model predictions vs. EPA AIRS observations for August 24, 2000 at 22:00 GMT.